



HAL
open science

No compelling evidence of distributed production of CO in comet C/1995 O1 (Hale-Bopp) from millimeter interferometric data and a reanalysis of near-IR lines

Dominique Bockelée-Morvan, Jérémie Boissier, Nicolas Biver, Jacques
Crovisier

► To cite this version:

Dominique Bockelée-Morvan, Jérémie Boissier, Nicolas Biver, Jacques Crovisier. No compelling evidence of distributed production of CO in comet C/1995 O1 (Hale-Bopp) from millimeter interferometric data and a reanalysis of near-IR lines. *Icarus*, 2010, 210 (2), pp.898. 10.1016/j.icarus.2010.07.005 . hal-00693827

HAL Id: hal-00693827

<https://hal.science/hal-00693827>

Submitted on 3 May 2012

HAL is a multi-disciplinary open access archive for the deposit and dissemination of scientific research documents, whether they are published or not. The documents may come from teaching and research institutions in France or abroad, or from public or private research centers.

L'archive ouverte pluridisciplinaire **HAL**, est destinée au dépôt et à la diffusion de documents scientifiques de niveau recherche, publiés ou non, émanant des établissements d'enseignement et de recherche français ou étrangers, des laboratoires publics ou privés.

Accepted Manuscript

No compelling evidence of distributed production of CO in comet C/1995 O1 (Hale-Bopp) from millimeter interferometric data and a reanalysis of near-IR lines

Dominique Bockelée-Morvan, Jérémie Boissier, Nicolas Biver, Jacques Crovisier

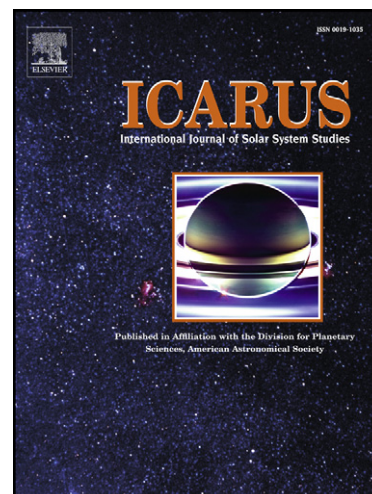
PII: S0019-1035(10)00277-0
DOI: [10.1016/j.icarus.2010.07.005](https://doi.org/10.1016/j.icarus.2010.07.005)
Reference: YICAR 9501

To appear in: *Icarus*

Received Date: 15 February 2010
Revised Date: 23 June 2010
Accepted Date: 6 July 2010

Please cite this article as: Bockelée-Morvan, D., Boissier, J., Biver, N., Crovisier, J., No compelling evidence of distributed production of CO in comet C/1995 O1 (Hale-Bopp) from millimeter interferometric data and a reanalysis of near-IR lines, *Icarus* (2010), doi: [10.1016/j.icarus.2010.07.005](https://doi.org/10.1016/j.icarus.2010.07.005)

This is a PDF file of an unedited manuscript that has been accepted for publication. As a service to our customers we are providing this early version of the manuscript. The manuscript will undergo copyediting, typesetting, and review of the resulting proof before it is published in its final form. Please note that during the production process errors may be discovered which could affect the content, and all legal disclaimers that apply to the journal pertain.



**No compelling evidence of distributed production of CO in comet
C/1995 O1 (Hale-Bopp) from millimeter interferometric data
and a reanalysis of near-IR lines**

Dominique Bockelée-Morvan

LESIA, Observatoire de Paris, F-92195 Meudon, France

dominique.bockelee@obspm.fr

Jérémie Boissier

IRAM, 300 rue de la Piscine, Domaine universitaire, F-38406, Saint Martin d'Hères, France

Nicolas Biver

LESIA, Observatoire de Paris, F-92195 Meudon, France

and

Jacques Crovisier

LESIA, Observatoire de Paris, F-92195 Meudon, France

Received _____; accepted _____

submitted second revised version to Icarus (July 13, 2010)

Running head : CO in comet Hale-Bopp

Number of pages : 55

Number of Tables : 3

Number of figures : 13

Key words: comet Hale-Bopp; Comets, composition; Radio observations; Infrared observations

Send correspondence to:

Dominique Bockele-Morvan

Observatoire de Meudon

5 place Jules Janssen

F92195 Meudon, Cedex, France

Phone : 33 1 45 07 76 05

ABSTRACT

Based on long-slit infrared spectroscopic observations, it has been suggested that half of the carbon monoxide present in the atmosphere of comet C/1995 O1 (Hale-Bopp) close to perihelion was released by a distributed source in the coma, whose nature (dust or gas) remains unidentified. We re-assess the origin of CO in Hale-Bopp's coma from millimeter interferometric data and a re-analysis of the IR lines.

Simultaneous observations of the CO $J(1-0)$ (115 GHz) and $J(2-1)$ (230 GHz) lines were undertaken with the IRAM Plateau de Bure interferometer in single-dish and interferometric modes. The diversity of angular resolutions (from 1700 to 42 000 km diameter at the comet) is suitable to study the radial distribution of CO and detect the extended source observed in the infrared. We used excitation and radiative transfer models to simulate the single-dish and interferometric data. Various CO density distributions were considered, including 3D time-dependent hydrodynamical simulations which reproduce temporal variations caused by the presence of a CO rotating jet. The CO $J(1-0)$ and $J(2-1)$ observations can be consistently explained by a nuclear production of CO. Composite 50:50 nuclear/extended productions with characteristic scale lengths of CO parent $L_p > 1500$ km are rejected.

Based on similar radiation transfer calculations, we show that the CO $v = 1-0$ ro-vibrational lines observed in comet Hale-Bopp at heliocentric distances less than 1.5 AU are severely optically thick. The broad extent of the CO brightness distribution in the infrared is mainly due to optical depth effects entering in the emitted radiation. Additional factors can be found in the complex structure of the CO coma, and non-ideal slit positioning caused by the anisotropy of dust IR emission.

We conclude that both CO millimeter and infrared lines do not provide compelling evidence for a distributed source of CO in Hale-Bopp's atmosphere.

Keywords: Comet Hale-Bopp – Comets, composition – Radio observations – Infrared observations

1. Introduction

About two dozen molecules have been detected in cometary atmospheres in addition to a wealth of radicals, atoms and ions formed by photodissociation, photoionization and coma chemistry (Bockelée-Morvan et al. 2004; Feldman et al. 2004). It is generally agreed that most molecules found in the coma are released from the nucleus, being present in condensed form or as trapped gases in water ice. However, there are pieces of evidence that distributed sources (also called "extended sources") of gas are present in cometary atmospheres (see the reviews of Bockelée-Morvan and Crovisier 2002; Cottin and Fray 2008). Molecules released from the nucleus and from extended sources exhibit different radial distributions in the coma. Molecules produced from the thermal or photo-degradation of organic grains should display characteristic production curves versus heliocentric distance (Fray et al. 2006). Radial distributions not consistent with nucleus production were found for H_2CO , CO , and OCS (e.g., Meier et al. 1993; DiSanti et al. 2003; Dello Russo et al. 1998). Strong heliocentric variations of the H_2CO , HNC , and CS mixing ratios were measured, suggesting a temperature-dependent production mechanism for these species (e.g., Biver et al. 1999b; Fray et al. 2006; Milam et al. 2006; Lis et al. 2008). The production of radicals (CN , C_2) from grains is also suggested. The study of extended sources of gases can provide important clues to the chemical nature of refractory organic compounds in cometary nuclei (Cottin and Fray 2008). For example, laboratory experiments show that the decomposition of polyoxymethylene, a polymer of formaldehyde, can be the source of monomeric H_2CO in cometary atmospheres (Cottin et al. 2004; Fray et al. 2006).

The first evidence for an extended CO production was obtained from measurements of the local CO density in comet 1P/Halley along the path of the Giotto spacecraft acquired with the neutral mass spectrometer (NMS). Eberhardt et al. (1987) concluded that only about one-third of the CO was released from the nucleus, the remainder being produced by an extended source in the coma. The total CO production rate in comet 1P/Halley was estimated to be 11% that of water at the time of the Giotto flyby (Eberhardt et al. 1987). An alternative view, that Giotto flew through a jet enriched in CO , was proposed by Greenberg and Li (1998) to interpret the NMS

observations.

Constraining the radial distribution of CO in cometary atmospheres from telescopic observations requires significant spatial resolution and a productive comet. Long-slit spectroscopic CO observations near $4.7 \mu\text{m}$ performed at $r_h < 1.5$ AU in comet C/1995 O1 (Hale-Bopp) have suggested that 50 to 90 % of the CO in this comet was originating from a distributed source (DiSanti et al. 1999; DiSanti et al. 2001; Brooke et al. 2003). Similar observations performed in C/1996 B2 (Hyakutake) indicate that CO was released almost entirely ($\sim 75\%$) from the nucleus (DiSanti et al. 2003). CO was abundant in these two comets with a total CO production rate $\sim 20\%$ relative to water.

We present here the study of the radial distribution of CO in comet Hale-Bopp from observations of the $J(1-0)$ (115 GHz) and $J(2-1)$ (230 GHz) lines undertaken with the IRAM Plateau de Bure interferometer (PdBI) (Bockelée-Morvan et al. 2009). Observations were performed both in single-dish and interferometric modes with angular resolutions probing coma radii from 830 to 20800 km, which encompass the characteristic scale (5000 km) of the CO extended source identified by DiSanti et al. (2001) and Brooke et al. (2003). Hence, they are appropriate for the study of the origin of CO gas in Hale-Bopp's coma.

There is observational evidence that the infrared CO ro-vibrational lines observed by DiSanti et al. (2001) and Brooke et al. (2003) in comet Hale-Bopp are optically thick. Optical depth effects make brightness radial profiles flatter than when optically thin conditions apply, and can lead to misinterpretations if they are not properly taken into account. We present a re-analysis of these lines using radiative transfer calculations.

Both the radio and IR CO data show evidence for the presence of a strong spiralling CO jet when comet Hale-Bopp was close to perihelion (Bockelée-Morvan et al. 2009; Brooke et al. 2003). This feature is considered in the present study.

The observations of the CO radio lines are summarized in Sect. 2.1; the methods and models used for their analysis are described in Sect. 2.2, and the results are given in Sect. 3. The analysis

of the infrared lines is presented in Sect. 4. A summary follows in Sect. 5.

2. Analysis of the CO millimetric data

2.1. Observations : summary

The detailed description of the observations of the CO $J(1-0)$ (115 GHz) and $J(2-1)$ (230 GHz) lines undertaken in comet Hale-Bopp with the IRAM PdBI can be found in Henry (2003); Bockelée-Morvan et al. (2009). They were performed on 11 March 1997 from 4.4 to 13.8 h UT. Comet Hale-Bopp was at a heliocentric distance of 0.989 AU and a geocentric distance of 1.368 AU. Both lines were observed simultaneously using different receivers and a spectral resolution of 0.13 km s^{-1} . At that time, the PdBI comprised five 15-m dishes. The interferometer was used in a compact configuration C1, with baselines (the spacing between two antennas), ranging from ~ 20 to ~ 150 m. Most of the time, the comet was observed in cross-correlation (interferometric) mode. However, every one hour short-time (1 min on source) single-dish observations (also referred as to ON-OFF measurements) were performed. The observing mode was position-switching to cancel the sky background, with the reference position taken at $5'$ from the comet position.

When all interferometric data are considered, the full width at half maximum (FWHM) of the synthesized interferometric beam is $2'' \times 1.38''$ at 230 GHz, and $3.58'' \times 2.57''$ at 115 GHz. The FWHM of the primary beam of the antennas is $20.9''$ at 230 GHz and $41.8''$ at 115 GHz. Given the geocentric distance of the comet, these angular resolutions correspond to projected distances of 1650 to 41600 km (diameter). Interferometric maps of the CO $J(1-0)$ and $J(2-1)$ emissions are presented in Bockelée-Morvan et al. (2009). The signal-to-noise ratio in the center of the maps ranges from 25 ($J(1-0)$) to 140 ($J(2-1)$). Line areas (i.e., flux densities integrated over velocity in units of Jy km s^{-1} , the lines being Doppler-resolved) measured on the overall single-dish (ON-OFF) spectra averaging all data (F_{SD}), and measured at the peak of interferometric maps (F_{Int}), are given in Table 1. For both ON-OFF and interferometric data, the uncertainties in flux calibration are at most 10% and 15% for the $J(1-0)$ and $J(2-1)$ lines,

respectively (Bockelée-Morvan et al. 2009).

2.2. Methods of analysis

The possible extended origin of CO can be investigated by comparing single-dish F_{SD} and interferometric F_{Int} fluxes (Table 1). Extended source production, if resolved out by the interferometric beam, would result in a ratio $R = F_{\text{SD}}/F_{\text{Int}}$ higher than the value expected for a pure nuclear production. On the other hand, opacity effects need also to be carefully investigated: being more important for smaller beams, they increase the $F_{\text{SD}}/F_{\text{Int}}$ intensity ratio with respect to optically thin conditions. The measured intensity ratios R_{1-0} and R_{2-1} (the subscripts refer to the lines) are given in Table 1, with error bars including uncertainties in flux calibration.

The CO radial distribution can also be studied from the brightness distribution observed in the interferometric maps. We preferred to study the direct output of the interferometer, i.e., the complex visibilities measured by the antenna pairs which sample the Fourier transform of the brightness distribution in a number of points in the Fourier plane (also called uv -plane). This approach allows us to avoid uncertainties in map analysis related to: 1) the ellipticity of the interferometric beam which results from the anisotropic coverage of the Fourier plane; 2) flux losses expected for extended sources due to the non coverage of the uv -plane at baselines shorter than 20 m. Visibilities (integrated over velocity) recorded by the ten baselines over the whole observing period were radially averaged in the uv -plane over intervals of uv -radius σ of 5 m (the uv -radius corresponds to the baseline length projected onto the plane of the sky). The line area determined on the averaged single-dish spectrum provides the visibility at $\sigma = 0$.

The visibility from extended source emission is expected to drop faster with increasing σ than for more compact sources. As shown in the Appendix, for a density distribution varying according to r^{-2} , where r is the distance to the nucleus, the amplitude of the visibility $\bar{\mathcal{V}}$ is expected to vary according to σ^{-1} , provided molecular excitation is not varying in the coma and the line is optically thin. For an optically thick line, the power index of the variation of $\bar{\mathcal{V}}$ with σ will be < -1 . For an

extended density distribution which follows a Haser daughter distribution, we computed that $\bar{V} \propto \sigma^{-2}$, if the parent scale length L_p is larger than the size of the interferometric beam and the line is optically thin. If molecular excitation is varying in the coma (e.g., as a result of variations of the gas kinetic temperature), $\bar{V}(\sigma)$ will deviate from these laws. The measured variation is $\propto \sigma^{-1.27 \pm 0.02}$ and $\propto \sigma^{-0.85 \pm 0.06}$, for the $J(2-1)$ and $J(1-0)$ lines, respectively (slightly different values were derived from linear fitting by Bockelée-Morvan et al. 2009).

These two approaches were used by Boissier et al. (2007) to study the radial distributions of H_2S , SO , and CS observed with the IRAM PdBI.

2.3. Modelling

Synthetic ON-OFF spectra and visibility spectra were computed using an excitation model and a radiative transfer code, following Boissier et al. (2007). We summarize here the main aspects of the computations.

The calculation of the population of the rotational levels of the CO molecules considers collisions with H_2O and electrons, and IR radiative pumping of the $v(1-0)$ CO vibrational band (Crovisier and Le Bourlot 1983; Crovisier 1987; Biver et al. 1999b). The model provides populations as a function of radial distance r , given a H_2O density law with r . For simplicity, we assumed an isotropic H_2O coma. The collisional CO- H_2O cross-section is taken equal to $\sigma_c = 2 \times 10^{-14} \text{ cm}^2$ (Biver et al. 1999b), and the H_2O production rate is $Q_{\text{H}_2\text{O}} = 10^{31} \text{ s}^{-1}$ (Colom et al. 1999). As shown in Bockelée-Morvan et al. (2009), PdBI observations, including ON-OFF measurements, were mostly sensitive to CO molecules with rotational populations at local thermal equilibrium (LTE). The large size of the CO LTE region can be explained by the high collisional rates in this productive comet and the large radiative lifetimes of the CO $J = 1, 2$ rotational levels.

Two nominal gas kinetic temperature laws were investigated: 1) a constant gas kinetic temperature throughout the coma equal to 120 K, which agrees with temperature determinations

pertaining to the $r \sim 10\,000$ km coma region (Biver et al. 1999a; DiSanti et al. 2001); this temperature provides a best fit to the relative intensities of the CO $J(2-1)$ and $J(1-0)$ lines measured in single-dish mode at PdBI (Bockelée-Morvan et al. 2009), assuming pure CO nuclear production and an isothermal coma; 2) a temperature law T_{var} increasing with increasing cometocentric distance, as expected from coma hydrodynamical models which include photolytic heating (Combi et al. 1999). The long-slit infrared spectroscopic observations of CO and other molecules undertaken in March-April 1997 in comet Hale-Bopp suggest typical gas kinetic temperatures of $\sim 80-90$ K at $r \sim 1000$ km (Magee-Sauer et al. 1999; DiSanti et al. 2001). We adopted the temperature law used by Boissier et al. (2007) to interpret the PdBI observations of sulfur-bearing species. It yields $T \leq 70$ K at $r \leq 1000$ km and $T = 120$ K at $r \geq 10\,000$ km (see footnote in Table 2). For a few calculations, we investigate an alternate temperature law $T_{\text{var(alt)}}$ with $T_{\text{var(alt)}} = T_{\text{var}}$ for $r \geq 1500$ km and $T = 79$ K for $r \leq 1500$ km.

In most calculations, the CO density distribution was computed using simple steady state isotropic models. We considered outflow either at a constant velocity (i.e., Haser models) or at a velocity which increases with increasing cometocentric distance. Indeed, gas acceleration is expected in the $r = 1000-10\,000$ km region probed by the PdBI in the Hale-Bopp coma, as a result of photolytic processes (Combi et al. 1999). The shape of radio lines provides constraints on the gas expansion velocity v_{exp} (e.g., Hu et al. 1991). From the width of radio lines of parent molecules (including CO) observed by single-dishes, Biver et al. (1999a) derived a value equal to 1.05 km s^{-1} for the period pertaining to the PdBI CO observations. This value is representative of the gas velocity at cometocentric distances of typically the radius of the field of view and therefore pertains to radial distances $\sim 10\,000$ km. The width of the CO lines in the interferometric beam suggests that $v_{\text{exp}} \sim 0.9 \text{ km s}^{-1}$ at $r \sim 1000$ km. For comparison, the model of Combi et al. (1999) yields to an acceleration from 0.91 to 1.12 km s^{-1} in the $r = 1000-10\,000$ km region, in good agreement with our velocity retrievals. For the models with constant velocity (v_{const}), we adopted $v_{\text{exp}} = 1.05 \text{ km s}^{-1}$. For the models which consider the variation of the velocity (v_{var}), we assumed $v_{\text{exp}} = 0.9 + 0.15 \times \log(r[\text{km}]/1000) \text{ km s}^{-1}$ for $r > 1000$ km, $v_{\text{exp}} = 0.9 \text{ km s}^{-1}$ for

$r < 1000$ km. Figure 1 shows the H_2S 2_{20-211} line at 216.7 GHz observed in comet Hale-Bopp on 13 March 1997 with the PdBI (Boissier et al. 2007). Synthetic line profiles computed with the v_{var} velocity law are superimposed. The width and wings of both the ON-OFF and interferometric spectra are reproduced. The spectral asymmetries present in the central part of the observed H_2S spectra are due to spatial asymmetries in the coma. CO and H_2S are expected to expand at the same expansion velocity. We checked that the v_{var} law consistently explains the width and wings of the CO $J(1-0)$ and $J(2-1)$ line profiles.

In theory, cometary line shapes contain information on the radial distribution of the molecules. Daughter molecules are expected to exhibit double-horn line shapes when the size of the beam does not exceed much their production scale length. The missing flux in the center of the line depends on the ratio of these two quantities. However in comet Hale-Bopp, CO line profiles were found to be affected by the presence of a CO rotating jet which introduced excess emission alternatively in the blue and red part of the profiles during the rotation (Bockelée-Morvan et al. 2009; Boissier et al. 2010). Such complexity prevents detailed fitting of the CO line shapes.

Extended distributions were investigated using the Haser formula for daughter species with the parent and daughter scale lengths L_p and L_d and the gas velocity v_{exp} as parameters. For simplicity, both L_p and L_d ($= L_{\text{CO}}$) were assumed to be constant throughout the coma, i.e., we did not consider the effect of the variation of the expansion velocity on the scale lengths. Therefore, in all calculations we assumed $L_{\text{CO}} = v_{\text{exp}}/\beta_{\text{CO}}$, with $v_{\text{exp}} = 1.05 \text{ km s}^{-1}$ and $\beta_{\text{CO}} = 7.5 \times 10^{-7} \text{ s}^{-1}$ (Huebner et al. 1992). Such approximation has a negligible effect on the results. Indeed, the CO scale length is much larger than the field of view of the single-dish measurements, so the CO column density within the field of view is not much affected by small inaccuracies in the effective CO scale length. The relative contribution of the extended and nuclear productions of CO is given by the ratio of the production rates $Q_{\text{CO}}^N:Q_{\text{CO}}^E$, where the subscripts N and E refer to the nuclear and extended productions, respectively. The total production rate is $Q_{\text{CO}}=Q_{\text{CO}}^N+Q_{\text{CO}}^E$.

We also consider in Sect. 3.3 much complex distributions where a large fraction of the CO production is within a spiralling jet. As mentioned above, a strong CO jet was indeed identified

in the coma of comet Hale-Bopp from these interferometric observations. The CO distribution is modelled using tridimensional, time-dependent codes (Bockelée-Morvan et al. 2009; Boissier et al. 2010).

The brightness distribution of the two CO lines was computed using the radiative transfer code of Boissier et al. (2007), which includes both self-absorption and stimulated emission (see Biver 1997, for detailed explanations). ON-OFF synthetic spectra were obtained by convolving the brightness distributions with the primary beam pattern of the PdBI antennas, described by a 2D Gaussian. Visibilities were calculated from the Fourier transform of the brightness distribution (Boissier et al. 2007). Maps of the CO line emissions were synthesized, considering the coverage of the Fourier plane obtained during the observations. The peak flux densities in the modelled and observed maps, both obtained by inverse Fourier Transform, can then be directly compared.

3. The CO radial distribution from millimetric data

3.1. ON-OFF and interferometric flux densities

Table 2 gives flux densities and intensity ratios $R_{Mod} = F_{SD}/F_{Int}$ computed with $Q_{CO} = 2.1 \times 10^{30} \text{ s}^{-1}$ and several Haser distributions describing the local CO density. Except for the first entry, corresponding to optically thin assumptions, all results were obtained with radiation transfer calculations.

The value $Q_{CO} = 2.1 \times 10^{30} \text{ s}^{-1}$ was chosen so that the $J(1-0)$ and $J(2-1)$ ON-OFF line intensities computed with $T = 120 \text{ K}$, a constant velocity and a pure CO nuclear production match precisely the measurements. This value is consistent with the total CO production rate (sum of native and extended distributions) inferred from IR spectroscopy (DiSanti et al. 2001). The other models considered in Table 2 yield ON-OFF line intensities consistent with the measured values if one takes flux uncertainties into account.

To quantify the goodness of the models in explaining the observed intensity ratios R_{Obs} (R_{1-0}

or R_{2-1}), we computed for both lines the quantity:

$$\chi^2 = (R_{\text{Obs}} - R_{\text{Mod}})^2 / \Delta R_{\text{Obs}}^2 \quad (1)$$

where ΔR_{Obs} is the uncertainty on R_{Obs} given in Table 1 and R_{Mod} is the intensity ratio given by the models. Results are plotted in Fig. 2. Models resulting in $\chi^2 > 1$ in either line are considered as non satisfactory.

3.1.1. Models with pure nuclear production

The $J(2-1)$ line observations can be fully interpreted by a nuclear CO production, provided the opacity effects are taken into account. Opacity affects mainly the flux density of the $J(2-1)$ line in the interferometric beam: e.g., a reduction by 37% is observed for the model with constant temperature and velocity, while ON-OFF $J(2-1)$ flux and $J(1-0)$ fluxes are almost unchanged (compare the first two entries in Table 2). When line opacity is considered, the R_{2-1} values obtained with either of the temperature and velocity laws ($\sim 18-19$) are consistent with the measured value of 17.8 ± 3.8 . χ^2 values close to zero are obtained (Fig. 2).

On the other hand, models considering a nuclear production and a constant gas kinetic temperature fail to explain the ratio $R_{1-0} = 11.6 \pm 1.8$ measured for the $J(1-0)$ line, yielding values 20–35% higher than observed. The discrepancy obtained for R_{1-0} cannot be solved by invoking an extended CO production because this process affects the intensity ratio in the opposite way (Fig. 2). However, a good agreement is obtained when the variable temperature law is used: the population of the $J = 1$ CO rotational level increases with decreasing T , hence producing an enhancement of the $J(1-0)$ emission from the inner colder parts. The R_{2-1} ratio is less sensitive to the assumed gas temperature law because the increase of $J(2-1)$ local emission in the inner regions is counterbalanced by more significant self-absorption effects for the emergent emission.

The R_{1-0} and R_{2-1} ratios are both sensitive to the assumed velocity law which affects the CO density radial profile. R_{1-0} decreases when the expansion velocity in the inner coma decreases, the outflow velocity at $r > 10\,000$ km being kept constant. R_{2-1} displays a non monotonous trend

with decreasing inner coma velocity $v_{\text{exp}}(\text{inner})$, slowly decreasing for $0.9 \text{ km s}^{-1} < v_{\text{exp}}(\text{inner}) < 1.05 \text{ km s}^{-1}$ (Table 2), and then increasing for $v_{\text{exp}}(\text{inner}) < 0.9 \text{ km s}^{-1}$. We found that it is not possible to explain both R_{1-0} and R_{2-1} measured ratios with a variable velocity law and a constant gas kinetic temperature.

In summary, the measured intensity ratios R_{1-0} and R_{2-1} can be explained with a CO nuclear origin when the variation of the gas kinetic temperature with distance to nucleus is considered.

3.1.2. Models with extended CO production

Let us first compare the measurements to model results obtained with pure CO daughter Haser distributions. Indeed, Brooke et al. (2003) interpreted long-slit infrared observations of CO in comet Hale-Bopp, with $\sim 90\%$ of the CO being released from a source with $L_p = 5000 \pm 3000$ km. We investigated CO parent scale lengths up to $L_p = 5000$ km. Such CO distributions with $L_p > 500$ km do not fit the data (Fig. 2). In other words, both the CO $J(1-0)$ and $J(2-1)$ data exclude that CO is produced solely by an extended source, unless this source releases most of the CO gas in the near-nucleus coma unresolved by the interferometric beam. Results obtained with $Q_{\text{CO}}^N:Q_{\text{CO}}^E$ in ratio 10:90 and $L_p = 5000$ km do not reproduce the measurements (Table 2), and thereby do not support the conclusions of Brooke et al. (2003).

DiSanti et al. (2001) interpreted the radial profiles of CO infrared emission by the contribution of a distributed source to 50 % of the total CO production. Therefore, we also investigated composite nuclear:extended productions with CO and CO parent production rates in ratio 50:50 (Table 2, and left part of the plots shown in Fig. 2). Satisfactory fits to both lines can only be obtained for models with the variable temperature law: the R_{1-0} and R_{2-1} ratios can be reproduced within $1-\sigma$ providing $L_p < 1000$ km (model with constant velocity) or $L_p < 2000$ km (model v_{var}). One can consider that the condition $\chi_{1-0}^2 + \chi_{2-1}^2 < 1$ should be satisfied as the $J(1-0)$ and $J(2-1)$ measurements are independent. Then, models with $L_p < 1500$ km (v_{var} law) and $L_p < 800$ km (v_{const} law) provide a satisfactory fit to the PdBI CO data based on the ratios

R of single-dish to interferometric fluxes. Since the adopted v_{var} law is consistent both with line shape measurements and gas dynamics calculations (Sect.2.3), we conclude that composite 50:50 nuclear/extended productions with $L_p > 1500$ km are excluded by the CO millimeter data.

It is worth noting that, using the models with the v_{var} and T_{var} laws, and extended productions fitting the data, we infer total CO production rates within 5% of the nominal value of $2.1 \times 10^{30} \text{ s}^{-1}$.

Still, we assumed isotropic CO density distributions. In Sect. 3.3, we discuss how the $F_{\text{SD}}/F_{\text{Int}}$ ratio is affected by the presence of jets.

3.2. Radial evolution of the visibilities

In Figs 3–4 are plotted the visibilities $\bar{\mathcal{V}}$ as a function of uv -radius σ expected for different models, together with the measurements. The power index of the variation of $\bar{\mathcal{V}}(\sigma)$ with σ measured on the modelled curves is given in Table 2. The least-squares fit to the computed visibilities was performed on an extracted set of visibilities representative of the σ sampling of the observations. Weighting factors corresponding to the uncertainties in the measured visibilities were considered when fitting the extracted set of computed visibilities. This method is appropriate for best comparison with the data, since the model results show that the visibility curves do not follow a simple power law (Fig. 4).

From visual comparison between the modelled and observed visibility curves (Figs 3–4), we see that :

1. Both lines exclude pure CO production from an extended source, unless the characteristic parent scale length of the distributed source is well below 500 km;
2. Composite nuclear/extended productions with $L_p = 5000$ km or 2000 km do not explain the observations.

3. The best fits are obtained for a nuclear production.

From a least square fitting of the visibility curves, including the ON-OFF point, we found that composite 50:50 nuclear/extended productions with $L_p > 1500$ km are not statistically favored when the v_{var} law is considered. In other words, we obtained the same results as derived from the intensity ratios.

Let us now compare the power indexes of modelled visibility curves to the measured values. For the $J(1-0)$ line, there is a good agreement (within 1.3-sigma) between the measured value and that given by the model with a nuclear CO production, and T_{var} and v_{var} laws. On the other hand, the same model predicts a power index of -1.40 for $J(2-1)$ whereas the measured value is -1.27 ± 0.02 . The steep decrease of the $J(2-1)$ visibility curve obtained with the T_{var} law at large uv -radii (> 70 m, see Fig. 4) is caused by large self-absorption effects in the inner cold coma observed by the interferometric beam ($r < 850$ km) where $T < 65$ K. At 230 GHz, uv -radii between 70–150 m probe cometocentric distances ($\propto \lambda/\sigma$) to which 115 GHz measurements are not sensitive. Unlike $J(2-1)$ visibilities, $J(1-0)$ visibilities are not influenced by the coma temperature at $r < 1500$ km. Figure 5 shows that the $J(2-1)$ data at large uv -radii can be better fitted using the alternate temperature law $T_{\text{var}(alt)}$ introduced in Sect. 2.3 for which $T = 79$ K at $r < 1500$ km and $T = T_{\text{var}}$ at $r > 1500$ km. The power index of the visibility curves computed with this alternate temperature law are -1.35 and -0.98 for $J(2-1)$ and $J(1-0)$ (Table 2), respectively, in reasonable agreement with the measurements. We plot in Fig. 6 curves of χ^2 values obtained with the $T_{\text{var}(alt)}$ law, which are analogous to those shown in Fig. 2.

The model with composite 50:50 nuclear/extended production and $L_p = 5000$ km closely reproduces the $J(2-1)$ measured power index, but not the flux ratio R_{2-1} (Table 2). It is unable to explain either the power index of the $J(1-0)$ visibility curve and R_{1-0} . This shows that best constraints on the radial distribution of CO are obtained from the comparison of ON-OFF and interferometric flux measurements.

3.3. Models with anisotropic CO production

A question that may arise is the extent to which our approach is appropriate in presence of jets in the coma. A spiralling CO jet comprising $\sim 30\%$ of the total CO production was identified from these PdBI data (Bockelée-Morvan et al. 2009). This jet, found to be issued from a low latitude nucleus region and to be $\sim 40^\circ$ wide, caused temporal modulations in the visibilities recorded by each pair of antennas, which are still visible in the radial and time averages shown in Fig. 3 and 4.

The question has been thoroughly studied for spiralling jets of various strengths and latitudes in the assumption of negligible optical depth and a constant coma temperature (Henry 2003). Henry (2003) used a simple description of the Hale-Bopp CO coma represented by the combination of an isotropic coma and a spiralling conical jet. These 3-D time dependent simulations show that, for nearly equatorial jets, the power index of the visibility curve remains close to -1 , except for collimated jets where the slope can reach -0.8 to -0.7 depending on the jet strength. An opposite trend is observed for high-latitude jets (see results obtained for optically thin conditions in Figs 20, 21 of Bockelée-Morvan et al. 2009). **These trends are explained by the sampling time of the measurements (2/3 of the nucleus rotation, i.e., almost one full rotation), the orientation of the different baselines with respect to the jet direction, and the shape of the modulations. The shortest baselines probed more particularly gas emissions along the rotation axis, while the longest baselines were sensitive to equatorial jets (see Figs 18 of Bockelée-Morvan et al. 2009). Hence, in presence of collimated equatorial jets, the slope of the visibility curve decreases. Simulations were not performed for the $J(1-0)$ line in presence of a CO jet (Henry 2003; Bockelée-Morvan et al. 2009). However, we do not expect conclusions different from those obtained for $J(2-1)$ since $J(1-0)$ and $J(2-1)$ were observed simultaneously, i.e., with the same baseline orientations. Less contrasted visibility modulations and slope variations are even expected for $J(1-0)$ in presence of jets, since the spatial resolution is degraded at 115 GHz.**

In the simulations of the CO PdBI data performed by Bockelée-Morvan et al. (2009), optical depth effects are considered and the kinetic temperature is assumed to be equal to 120 K. When the jet parameters that provide the best fit to the data are considered (jet model (3)), the power index of the $J(2-1)$ visibility curve agrees with that measured on the observed visibilities (Bockelée-Morvan et al. 2009).

We also investigated to which extent the flux ratio R_{21} is affected by the presence of the CO jet. A value of 18.4, consistent with observations, is derived from the synthesized interferometric maps obtained by Bockelée-Morvan et al. (2009) with their jet model (3). Other model simulations are worth to consider. In contrast to the simple description of the coma made by Henry (2003) and Bockelée-Morvan et al. (2009), Boissier et al. (2010) simulated the CO PdBI observations of comet Hale-Bopp using a tridimensional time-dependent gas-dynamical model of the coma. An increased CO production from a localized region on the nucleus surface is considered to produce the observed CO spiralling structure. R_{21} values in the range 18–18.6 are inferred from their solutions 3–5 which provide the most satisfactory fits to the data. These values are comparable to the values found under the assumption of isotropic CO production (Table 2) and to the observed value.

4. The CO radial distribution from infrared data

4.1. General considerations

The millimetric and infrared CO data lead apparently to inconsistent results concerning the origin of CO in Hale-Bopp’s coma. Based on radiative transfer calculations of CO $v = 1-0$ ro-vibrational line emission at $4.7 \mu\text{m}$, we argue that the analyses of DiSanti et al. (2001) and Brooke et al. (2003) were hampered by an improper account of the opacity of these lines.

Qualitatively, opacity effects are an attractive explanation:

- Being more important for the central pixels aimed at the inner coma, they make line

brightness radial profiles to be flatter than when optically thin conditions apply, and to mimic profiles for species with extended production;

- They are all the more important since the CO production rate is large and the geocentric distance is low. DiSanti et al. (2001) found that in comet Hale-Bopp the CO extended source was present for $r_h < 1.5$ AU (Q_{CO}/Δ in the range $5\text{--}16 \times 10^{29} \text{ s}^{-1}\text{AU}^{-1}$) and inactive for $r_h > 2$ AU ($Q_{\text{CO}}/\Delta < 1 \times 10^{29} \text{ s}^{-1}\text{AU}^{-1}$). Interestingly, comet Hyakutake was also a CO-rich comet and the CO infrared data showed extended brightness profiles when Q_{CO}/Δ was 1 to $5 \times 10^{29} \text{ s}^{-1}\text{AU}^{-1}$ (DiSanti et al. 2003). Since the optical thickness increases with decreasing gas kinetic temperature, one expects opacity effects to be relatively more prominent in the CO brightness profiles of comet Hyakutake where the gas temperature was measured to be smaller. We are not aware of any other comet observed by means of high-resolution infrared spectroscopy showing evidence of an extended CO distribution (DiSanti and Mumma 2009). So far, for all other comets studied to date in the infrared, Q_{CO}/Δ was much lower than $10^{29} \text{ s}^{-1}\text{AU}^{-1}$.
- Comparison of the intensity of lines emitted by a common ro-vibrational level provides direct evidence for significant opacity effects in the lines of sight passing close to the nucleus. Under optically thin conditions, the ratios of P2 to R0 (upper rotational level $J_u = 1$), and of P3 to R1 ($J_u = 2$) line intensities are equal to 2 and 3/2, respectively (i.e. $(J_u+1)/J_u$). Smaller values are observed, consistent with the higher absorption coefficients of the P2 and P3 lines as compared with those of R0 and R1, respectively (DiSanti et al. 2001). The radial brightness profile of R0 is less extended than those of R1, R2 and R3, which can be explained by the lower R0 absorption coefficient (see Fig. 13 of Brooke et al. 2003).

Opacity effects affect the fluorescence excitation of the CO $v = 1$ vibrational band in the inner coma, the solar photons being absorbed along their path. Opacity effects also result in self-absorption of infrared photons emitted by nearby CO molecules (radiation trapping), which counterbalances the reduced direct excitation by solar photons. Last, but not least, the received radiation can be severely decreased by self-absorption effects. DiSanti et al. (2001) considered

the attenuation of the solar pump and computed effective g-factors accounting for optical depth effects. They did not studied quantitatively the fate of emitted photons, and assumed optically thin lines. Using effective g-factors, their conclusions remained essentially unchanged concerning the extended source of CO in comet Hale-Bopp. DiSanti et al. (2003) found that the attenuation of the solar pump explains in large part the CO extended brightness profiles observed in comet Hyakutake, especially those obtained end of March 1996 at $\Delta = 0.1$ AU. Brooke et al. (2003) considered optical effects both in the solar pump and in the emitted radiation to explain data obtained on 5 March 1997, and found spatial profiles only slightly wider than in the optically thin case.

We note that, despite CO being less abundant than water, its $v = 1-0$ ro-vibrational lines are expected to be much thicker than the H₂O lines from hot bands observed in the infrared. Photons emitted from a ro-vibrational transition $(v', i) \rightarrow (v'', j)$ can only be re-absorbed by the (v'', j) level to excite (v', i) . In cometary atmospheres, most of the molecules are in their ground fundamental vibrational state. Hence, self-absorption is much less important for H₂O hot bands, which connect weakly populated high vibrational states, than for the CO $v = 1-0$ band. Using the infrared excitation model of Bockelée-Morvan and Crovisier (1989), we computed that the opacity of $\nu_3-\nu_2$ H₂O lines observed in comet Hale-Bopp (Dello Russo et al. 2000; Brooke et al. 2003) is typically 5-6 orders of magnitude lower than the opacity of CO $v = 1-0$ lines at 1 AU from the Sun. For example, we can compare the P3 ($J = 2 \rightarrow 3$) line of CO $v = 1-0$ (2131.6 cm^{-1}) to the $2_{12} \rightarrow 3_{03}$ line of H₂O $\nu_3-\nu_2$ (2003 cm^{-1}). The line absorption coefficient, and therefore the opacity, is proportional to the Einstein coefficient for absorption B_{ji} ($\propto A_{ij}$, the Einstein coefficient for spontaneous emission) times the population of the lower level of the transition n_j . Assuming that the rotational levels of the ground vibrational state are populated according to a Boltzmann distribution at 80 K, for the CO line we have $A_{ij} = 20.3 \text{ s}^{-1}$ and $n_j = 0.14$, while for the H₂O line $A_{ij} = 1.14 \text{ s}^{-1}$ and $n_j = 7.0 \cdot 10^{-6}$.

4.2. Modelling

We performed detailed calculations of CO $v = 1-0$ line intensities solving exactly the radiative transfer by integration through the coma. The source functions at each radial distance were determined using the escape probability formalism (Bockelée-Morvan 1987). This method allows one to solve the statistical equilibrium equations for the level populations decoupled from any radiative transfer. It accounts for absorption of nearby emitted photons, stimulated emission, and for the attenuation of the solar flux by a correction factor to the excitation rates. Zakharov et al. (2007) showed that the escape probability formalism is appropriate to account for radiation trapping in cometary atmospheres. Escape probabilities were computed assuming spherical expansion at constant velocity (Bockelée-Morvan 1987). The same approach was used by Brooke et al. (2003). To compute fluorescence excitation of the $v = 1$ vibrational band, the population distribution in the ground vibrational state is needed. We used the excitation model for rotational emission described in Sect.2.2. For completeness, collisional quenching of $v = 1-0$ fluorescence was considered assuming a collisional cross-section for de-excitation equal to $2.5 \times 10^{-16} \text{ cm}^2$, H_2O being the collision partner. However, this process was found unimportant for comet Hale-Bopp close to perihelion, except within a hundred of kilometers from the nucleus surface. Because of Doppler shifts, the optical depth experienced by the CO emitted photons depends on the velocity distribution and radial profile. As for the radiative transfer calculations of CO rotational line emission, constant or variable velocity radial profiles were assumed. The local velocity dispersion was described by thermal broadening.

Two radiative transfer codes were developed. In the first one, which results are presented in Sect.4.4, isotropic Haser distributions were considered. The second one is an adaptation of the code of Bockelée-Morvan et al. (2009) used to interpret the CO interferometric radio data (see Sect.3.3). The CO coma is modelled as the sum of an isotropic contribution and a spiralling jet. The gas velocity and temperature are assumed to be the same in the two components (see discussion in Boissier et al. 2010). Calculations performed with the second code are presented in Sect. 4.5.

4.3. Q-curve analysis

To study the extent to which the spatial distribution of compounds deviates from that expected for direct release from the nucleus, DiSanti et al. (2001) developed the method of Q -curves. An apparent production rate Q_{app} is derived from the intensity $F_{line}(x)$ measured at a specific location x along the slit, under the assumption of spherical outflow from the nucleus at constant velocity :

$$Q_{app}(x) = \frac{4\pi\beta\Delta^2 F_{line}(x)}{hc\nu g_{line} f(x)}, \quad (2)$$

where g_{line} is the line fluorescence g-factor, and β is the CO photodissociation rate. The quantity $f(x)$ represents the fraction of the total number of molecules in the coma within the region sampled at offset x . Q -curves trace the evolution of $Q_{app}(x)$ as a function of x (given in arc sec or in km with respect to the nucleus position). For direct release from the nucleus and optically thin conditions, Q -curves reach quickly a terminal value equal to the true molecular production rate. Q_{app} values measured at small offsets from the nucleus underestimate the true production rate as the measured intensities are here affected by slit losses due primarily to seeing (DiSanti et al. 2001). The ratio between the terminal and on-nucleus Q_{app} values is larger for extended brightness distributions than for more compact distributions. An extended distribution can be identified by comparing with Q -curves obtained for dust or species of purely nuclear origin observed in similar seeing conditions. To examine how optical depth effects may have affected the CO Q -curves, it is then important to take into account slit losses in our modelling.

4.4. Results with isotropic distributions

In this section, we present results obtained under the assumption of an isotropic CO coma. Figure 7 shows Q -curves computed for conditions corresponding to the data acquired on December 11, 1996 ($r_h = 2.02$ AU, $\Delta = 2.83$ AU, $Q_{CO} = 3.0 \times 10^{29} \text{ s}^{-1}$) and January 21, 1997 ($r_h = 1.49$

AU, $\Delta = 2.2$ AU, $Q_{\text{CO}} = 1.1 \times 10^{30} \text{ s}^{-1}$). Carbon monoxide is assumed to be solely released from the nucleus. The CO ro-vibrational lines used for generating these Q -curves are the same as those used by DiSanti et al. (2001) in their Fig. 7. According to DiSanti et al. (2001), the data of December 1996 are consistent with direct release of CO from the nucleus, whereas those of January provide evidence for production from an extended source. We convolved the modelled brightness distribution of CO $v = 1-0$ emission lines by a 2-D Gaussian representing the point spread function (PSF), and computed expected fluxes in $1 \times 1''$ boxes along the radial direction, for direct comparison with the data of comet Hale-Bopp presented by DiSanti et al. (2001). We assumed a seeing equal to $3''$ and $2.1''$ for modelling the December and January data, respectively. These values provide reference dust Q -curves (see below) consistent with those observed. The gas kinetic temperature was taken equal to 60 K (Dec. data) and 80 K (Jan. data), based on the temperature measurements in the outer coma from the CO IR lines (DiSanti et al. 2001). Calculations shown in Fig. 7 were performed under the assumption that the gas expansion velocity v_{exp} is constant throughout the coma and equal to 0.9 km s^{-1} (Dec. data) and 1.0 km s^{-1} (Jan. data) (Biver et al. 2002).

For each date, two Q -curves were generated: 1) a reference Q -curve (empty circles) where the lines were assumed to be optically thin, collision quenching of fluorescence emission was neglected, and the rotational level populations in the fundamental were assumed to be at LTE; this reference Q -curve is also representative of the expected Q -curve from dust, providing dust emission falls off as $1/\rho$, where ρ is the projected distance from the nucleus; 2) the second Q -curve (filled circles) was generated from the intensities computed with the full model. Apparent production rates were derived using Eq. 2 and g -factors at $T = 60$ K (Dec. data) and 80 K (Jan. data). The comparison of these Q -curves shows that the CO ro-vibrational line emission was severely affected by optical depth effects in January 1997 (Fig. 7). The terminal Q_{app} values for the scaled reference Q -curve and CO Q -curve are in ratio $R_Q = 0.56$. This is close to the measured value of 0.49 (DiSanti et al. 2001), showing that the opacity of the lines explain in large part the extended nature of the spatial brightness profiles. At the largest offsets plotted in the figure, Q_{app} is slightly below the true CO

production rate because opacity effects are still significant. As for the December conditions, the model predicts that opacity effects should be discernible on the Q -curve: the scaled reference Q -curve and CO Q -curve are predicted to be in the ratio $R_Q = 0.83$. Figure 8 plots the mean line opacity of several R and P lines for the conditions of early March 1997 ($\Delta = 1.47$ AU, $Q_{\text{CO}} = 2 \times 10^{30}$ s $^{-1}$, $T = 90$ K). The mean line opacity is a weighted-average of the opacities in spectral channels covering the Doppler-resolved line, where the weight is the intensity in the spectral channels. The opacity of the R6 line (4.9 for early March) drops to 2.2 and 0.5 for mid-January and mid-December, respectively. Note that the IR CO lines are generally much thicker than the radio lines (Fig. 8).

As discussed by DiSanti et al. (2001), a reduction of the opacity of the CO infrared lines may be expected if one considers gas acceleration. To investigate this effect, we solved the radiation transfer with gas accelerations consistent with the model of Combi et al. (1999). In the law used to interpret the December data, the gas velocity increases from 0.81 to 0.92 km s $^{-1}$ for radial distances between 1000 and 20 000 km. As for January, it increases from 0.81 (1000 km) to 1.03 km s $^{-1}$ (20 000 km). The results are shown in Fig. 9. A small reduction of the opacity effects is obtained. R_Q values are increased from 0.83 to ~ 0.90 and from 0.56 to 0.60, for December and January, respectively. We consider that the December data are satisfactorily explained by the model.

A 20% discrepancy between the computed and measured R_Q values remains for the January data, which indicates that the observed spatial profiles are slightly more extended than expected for a pure CO nuclear origin. Calculations of brightness profiles applying to the February to May 1997 data of DiSanti et al. (2001) show that a discrepancy of 20–30% is systematically present. Figure 10 shows Q -curves for January conditions generated with combined 50:50 nuclear/extended distributions and CO parent scale lengths L_p from 1500 to 5000 km. R_Q decreases from 0.56 to 0.45 for L_p increasing from 0 km (i.e., nuclear production) to 5000 km. Considering the reduction of opacity effects caused by gas acceleration, the best fit to the January data is obtained for $L_p = 5000$ km.

While we cannot exclude a contribution of a distributed source of CO, its presence is not so compelling. Indeed, spatial profiles of water obtained with the same high resolution infrared instrumentation were also found to be broader than dust profiles and profiles computed for a ρ^{-1} brightness distribution convolved with the PSF (Dello Russo et al. 2000). The differences between water and dust/PSF Q -curves are comparable to or larger than the differences between observed and computed (pure nuclear origin) CO profiles. Dello Russo et al. (2000) discussed several possible explanations for the different behaviors of water, dust and PSF Q -curves and could not conclude for the contribution of a distributed source of water. In the next section, we argue that the complexity of the CO and dust Hale-Bopp comas should be considered to fully explain the CO spatial profiles.

4.5. Model with anisotropic CO distribution

As mentioned earlier, close to perihelion the coma of comet Hale-Bopp was structured by a strong CO spiralling jet originating from a low latitude region in the northern hemisphere (Bockelée-Morvan et al. 2009). In contrast, the dust coma was dominated by a high latitude northern jet producing repetitive shells (Jorda et al. 1999; Vasundhara and Chakraborty 1999). This northern dust jet introduced a significant departure between the nucleus position and the center of brightness in visible images. Astrometric positions obtained around perihelion were all off by $\sim -3''$ in Declination with respect to the nucleus position (Boissier et al. 2007). The observations of the CO IR lines were performed with the slit centred on the peak signal in the continuum and aligned along the East-West direction (DiSanti et al. 2001; Brooke et al. 2003). Hence, they were likely not centred on the nucleus position.

These spatial East-West profiles presented complex asymmetric shapes, with the maximum of the emission frequently peaking at $1-2 \times 10^3$ km (typically $1-1.5''$) West or East of peak dust emission (DiSanti et al. 2001; Brooke et al. 2003). These complex shapes might be related to the CO rotating jet.

We performed 3D radiative transfer calculations for CO infrared lines using the coma model of Bockelée-Morvan et al. (2009). We present results obtained with their jet model (3) for the geometric conditions of early March 1997, $Q_{\text{CO}} = 2 \times 10^{30} \text{ s}^{-1}$ and $T = 90 \text{ K}$. Several sets of IR CO data have been acquired during this period (namely on March 1.08, 3.80 and 5.99 UT DiSanti et al. 2001; Brooke et al. 2003), which is close to the date (11 March) of the interferometric CO observations used to constrain this jet model. The jet is defined by its half-aperture ($\Psi = 18.3^\circ$), latitude ($\ell = 20^\circ$), and the fraction of CO molecules released within the jet ($f_{\text{co}} = 35.5\%$). In early March 1997, the spin axis had an aspect angle $\theta_\omega \sim 77^\circ$ and a position angle on the sky $pa_\omega \sim 205^\circ$ based on the spin orientation derived by Jorda et al. (1999). Figure 11 shows the expected brightness distribution of the R6 CO line as a function of time over one nucleus rotation period. The jet structure is aligned along the RA axis towards West during about half of the period. The brightness distribution is more extended along the jet. Using the longitude of the jet at the nucleus surface determined by Bockelée-Morvan et al. (2009) for 11 March UT and a synodic rotation period of $11.31 \pm 0.01 \text{ h}$ (Farnham et al. 1999; Jorda and Gutiérrez 2000), we inferred that the brightness distributions for 1.87, 3.80 and 5.99 March UT should be approximately those shown in panels 3, 4, and 11 of Fig. 11, respectively. Next, we will also consider panel 10 for comparisons with the 5.99 March UT data.

The 1.87 March UT spatial profile peaks East of the continuum peak and falls off less rapidly with increasing ρ towards West than towards East (DiSanti et al. 2001). This is consistent with spatial profiles extracted from panel 3 (Fig. 12). As for the spatial profiles of 3.80 and 5.99 March UT, the sign of the offset would match the data if the directions given in Brooke et al. (2003) were reversed. On 3.80 March the peak intensity is observed westward the continuum peak and is more extended towards East, while the model predicts the opposite (Fig. 12). This is puzzling because the time between the March 1.87 and 3.80 UT observations is 4.1 periods, so we expect the profiles to exhibit the same shape. For 5.99 March UT, the peak intensity is towards the East, but predicted towards West (panel 11). T. Brooke (personal communication) comments that it is possible that the orientations given in Brooke et al. (2003) are in error though he does not have

firm evidence.

Figure 12 displays extractions parallel to the East-West direction for several negative offsets δDec in Declination. The peak intensity decreases when the offset increases, so that the spatial profile broadens. The position of the centroid of the emission reaches 1 to $3.5''$ for the times corresponding to panels 3, 4 and 10. Very broad profiles are obtained for panel 11 (expected to represent 5.99 March data), because the jet is nearly in the plane of the sky and aligned along East-West at that time (Fig. 11).

The intensity at $12''$ normalized to the peak intensity is in the range 0.12–0.20 at $\delta\text{Dec} = 0''$, 0.13–0.25 at $\delta\text{Dec} = -1.2''$, and 0.15–0.30 at $\delta\text{Dec} = -2.4''$. Values as high as 0.3 ($\delta\text{Dec} = -1''$) and 0.5 ($\delta\text{Dec} = -2.5''$) are inferred in the West side of extractions from panel 2. For comparison, on the spatial profiles recorded in March–April 1997, this quantity generally ranges between 0.15–0.30, with extreme values of 0.10 and 0.4 being also observed. Therefore, the extended appearance of the CO brightness distribution could also be partly related to the positioning of the slit. Detailed modelling of the complex shapes of the CO IR radial profiles would be challenging. They are strongly sensitive to the jet characteristics and nucleus rotation properties. The time-dependent model of Bockelée-Morvan et al. (2009) provides a very simplistic description of Hale-Bopp’s rotating CO coma, and does not explain in detail the interferometric CO maps. More sophisticated models would be required, and this is beyond the scope of this paper.

So far, we did not discuss how the absolute intensities given by the model compare to the measurements. This exercise is possible for the data published by Brooke et al. (2003), as intensities are listed in the paper. Table 3 lists measured R2 and R6 line fluxes. Fluxes in a $2'' \times 1''$ inner box centred on the brightness peak (F_{inner}), and East-West averages of $5'' \times 1''$ boxes starting $3''$ from the flux peak (F_{outer}) are given. Results from model calculations are also given in Table 3 for three slit offsets in Declination ($\delta\text{Dec} = 0, -1.2, \text{ and } -2.4''$). To compare to the 5.99 March data, we show results obtained using the radial profiles from panel 10 instead of those from panel 11, as the latter are much broader than those observed. The measured line flux ratios F_{outer}/F_{inner} (~ 1.04 – 1.09 , Table 3) can be explained providing the slit was offset by

1–2'' in Dec from the nucleus position. The intensities measured on 3 March suggest that the CO production rate was higher than $2 \times 10^{30} \text{ s}^{-1}$ at that time. Using simple scaling, we infer a value consistent with the Brooke et al. (2003) determination of $2.6 \times 10^{30} \text{ s}^{-1}$ based on the line fluxes at large projected distances (outer box). The intensities measured on 5 March suggest a total CO production rate of $\sim 1.4 \times 10^{30} \text{ s}^{-1}$, consistent with the value derived by Brooke et al. (2003). Note that the IR H₂O observations performed on 5 March also suggest that comet Hale-Bopp was less active on that day (Brooke et al. 2003).

Table 3 provides also the intensities of the R2 and R6 lines obtained using a steady state isotropic model for the CO density distribution. The flux ratios F_{outer}/F_{inner} are, for most entries, slightly lower than the values obtained with the anisotropic model (i.e., the model with the jet yields East-West averaged radial profiles only slightly broader than for an isotropic coma). We computed that, for a seeing of 1.7, the expected F_{outer}/F_{inner} ratio for isotropic and optically thin conditions is 0.33, consistent with values measured for CH₄ and H₂O in early March for similar seeing values (Brooke et al. 2003). Hence, the broad spatial distribution of the CO IR line emission results mainly from optical depth effects and, at a lesser extent, from the anisotropy of the CO coma and non-ideal slit positioning.

Our conclusion is inconsistent with the one obtained by Brooke et al. (2003) using similar modelling, but isotropic CO distributions. Brooke et al. (2003) analysed the radial profile of the R6 line observed on 5 March, and were able to fit the flux in the inner box F_{inner} with $Q(\text{CO}) = 4 \times 10^{29} \text{ s}^{-1}$ and $T = 100 \text{ K}$. With such a low CO production rate, spatial profiles were only slightly broader than in the optically thin case. Using the same parameters, our model yields a value for F_{inner} which is 40% lower than the observed value, and a F_{outer}/F_{inner} ratio equal to 0.43, i.e., barely higher than the optically thin value. Our model requires a higher CO production rate to fit the observations, yielding more pronounced opacity effects. We were not able to elucidate the origin of the discrepancy between the two models.

4.6. Relative intensities of ro-vibrational lines

We now examine how optical depth effects affect the relative intensities of the CO $v=1-0$ ro-vibrational lines.

As already mentioned, for beams passing close to the nucleus, the ratio of the P2 to R0 line intensities was measured to be lower than the statistical value of 2 expected under optically thin conditions (DiSanti et al. 2001). The East-West averaged P2/R0 intensity ratio was found to approach the statistical ratio at distances $\rho > 2300$ km ($> 1.5''$) in January, and $\rho > 5800$ km ($> 5.5''$) in March–April. This trend can only be explained by opacity effects. As shown in Fig. 8, at the temperatures encountered in the Hale-Bopp coma, the opacity of the R0 line is smaller than the P2 line opacity (by a factor of 1.6 for January–April). Figure 13 plots the P2/R0 intensity ratio derived from our radiative transfer models for the two periods. The on-nucleus value of 1.55 found for early March agrees with (although somewhat higher) the measured value of $\sim 1.3 \pm 0.1$ derived from Fig. A1 of DiSanti et al. (2001), not considering the possible slit offset in Dec discussed in the previous section (in which case we may conclude that the model slightly underestimate optical depth effects). The computed evolution of the P2/R0 intensity ratio along the slit agrees with the measurements. As for January, radiative transfer calculations in the assumption of an isotropic coma lead to a P2/R0 ratio lower than the observed value ($\sim 1.3 \pm 0.2$). Our modelling does not predict a significant decrease of the P3/R1 intensity ratio with respect the optically thin statistical value of 1.5, because the two lines have approximately the same opacity (Fig. 8). A P3/R1 intensity ratio significantly lower than 1.5 was observed, however, but only in January (Fig. A1 of DiSanti et al. 2001). Overall, there are some indications that our modelling underestimates opacity effects, which strengthens our interpretation of the CO spatial profiles as being strongly affected by opacity effects.

In optical thin conditions, the rotational temperature T_{rot}^v describing the population distribution in the vibrational excited state can be retrieved from the relative intensities of the ro-vibrational IR lines. This temperature is close to the rotational temperature in the ground vibrational state T_{rot} , and probes the gas kinetic temperature when the field of view encompasses

essentially the collision-dominated coma. Applying the method of rotation diagrams to the CO Hale-Bopp data, DiSanti et al. (2001) retrieved T_{rot}^v for $v=1$, as a function of projected distance to nucleus. However, this method is in principle not appropriate since the CO lines are optically thick. We applied the same method to synthetic line fluxes, giving the same weight to all lines. We found that : i) $T_{rot}^v(meas.) \leq T_{rot}^v$, where $T_{rot}^v(meas.)$ is the value retrieved from the rotation diagram; ii) $T_{rot}^v(meas.)$ and T_{rot}^v differ by an amount which depends on the lines used in the rotation diagram; iii) T_{rot}^v is larger than T_{rot} in the ground vibrational state by typically 8–10%. For the December simulations performed with $T = 60$ K (R2–R3, P2–P3 lines), we found for the inner $1'' \times 1''$ box: $T_{rot}^v(meas.) = 60$ K, $T_{rot}^v = 66$ K; for the January simulations with $T = 80$ K (R0 to R6, P1 to P4 lines): $T_{rot}^v(meas.) = 65$ K, $T_{rot}^v = 86$ K. The rotation diagram method underestimates more significantly T_{rot}^v when the R0, R1 and P1 to P3 lines are considered, because these lines, which are pumped from the lowest energy $v = 0$ rotational states, are less optically thick than the other lines (Fig. 8). DiSanti et al. (2001) points out that the measured temperatures on 24 February 1997 are higher compared with those on most other dates. We suggest that this is because the P1 to P3 and R0–R1 lines were not used (they were not observed on 24 February). In summary, T_{rot}^v values derived from set of lines that include R0–R1 and P1 to P3 lines likely underestimate (by typically 10–15 K) the gas kinetic temperature T in the innermost lines of sight.

5. Summary

The high productivity of comet Hale-Bopp in carbon monoxide made possible the investigation of the spatial distribution of this molecule in the inner ($r = 1000$ – $10\,000$ km) coma by means of spectroscopy from ground-based telescopes. Because there was observational evidence of an extended production of CO in infrared data (DiSanti et al. 2001; Brooke et al. 2003), we performed a detailed analysis of the CO data acquired with the IRAM Plateau de Bure interferometer close to perihelion (March 1997) for a confirmation of this extended production. This study benefited from the simultaneous observations of two CO rotational lines, the combination of both high and low angular resolutions probing coma radii from ~ 800 to $\sim 20\,000$ km, and last but not least very

high signal-to-noise ratios. The results obtained from this study urged us to analyze the CO infrared data using radiative transfer codes similar to those used for interpreting the millimeter data. We reached the following conclusions:

1. Both $J(1-0)$ and $J(2-1)$ radio lines exclude pure CO production from an extended source, unless the characteristic parent scale length L_p of the distributed source was smaller than 500 km;
2. Composite models considering half of the CO production from a distributed source cannot explain the radio observations, unless L_p was < 1500 km. A good fit to the data is obtained when CO is assumed to be solely released from the nucleus;
3. The $J(1-0)$ line data are best explained when considering the radial evolution of the temperature in the coma due to photolytic heating. Secure results are obtained for the $J(2-1)$ line thanks to the development of a radiative transfer code which accounts for optical depth effects in the emergent emission;
4. The presence of a CO spiralling jet in the Hale-Bopp's coma does not affect much our analysis because the millimetric observations spanned a large fraction of the nucleus rotation and probed almost the whole coma at projected distances $\rho < 20\,000$ km;
5. The observed CO ro-vibrational lines are optically thick. The broad extent of the CO brightness distribution in the infrared is mainly due to optical depth effects entering in the emitted radiation. Surprisingly, our conclusion is not consistent with the one obtained by Brooke et al. (2003) who performed similar radiative transfer calculations. Comparison of model results shows that they quantitatively differ.
6. The slit-oriented spatial profiles of the CO infrared lines are strongly affected by the CO jet, making their interpretation difficult. They are more extended than expected for a pure nuclear origin possibly also because the slit was centred on the peak of the dust continuum emission which departed from the nucleus position.

7. The comparison between observed and computed P2/R0 line intensity ratios suggests that our modelling underestimates optical depth effects, which strengthens our interpretation of the broad extent of the IR emission.
8. When optical depth effects are present, the rotation diagram method introduces errors in rotational temperature determinations.

In conclusion, our analysis shows that there is no compelling evidence of extended production of CO in Hale-Bopp's coma. We anticipate that a similar conclusion should be reached for comet Hyakutake from a reanalysis of the observed IR lines.

Acknowledgements: IRAM is an international institute co-funded by the CNRS, France, the Max-Planck-Gesellschaft, Germany, and the Instituto Geográfico Nacional, Spain. This work has been supported by the Programme national de planétologie of Institut national des sciences de l'univers.

APPENDIX : Visibilities for long-lived parent molecules

In this Appendix, we demonstrate that, for a parent molecule distribution, the amplitude of the visibility $\bar{\mathcal{V}}(\sigma)$ varies with the uv -radius σ according to σ^{-1} , in first approximation.

Let us start from the general equation of the complex visibility $\mathcal{V}(u, v)$ that can be approximated to:

$$\begin{aligned} \mathcal{V}(u, v) &= \frac{c}{\nu} \int_{-\infty}^{+\infty} \int_{-\infty}^{+\infty} A(x, y) F(x, y) \\ &\times \exp\left(-\frac{2i\pi\nu}{c}(ux + vy)\right) dx dy \end{aligned} \quad (1)$$

in units of line area (Jy km s^{-1}). u and v are the coordinates of the baseline vector for two antennas in the uv -plane. $F(x, y)$ is the brightness distribution in the plane of the sky. $A(x, y)$ is the antenna primary beam pattern of half-power beam width θ_B , approximated by a 2-D Gaussian centred on $(0, 0)$ given by:

$$A(x, y) = \exp\left(-\frac{4 \ln(2)(x^2 + y^2)}{\theta_B^2}\right).$$

Under optically thin conditions and assuming that the population of the upper level of the transition p_u does not vary with distance to nucleus, $F(x, y)$ is proportional to $\int_{-\infty}^{+\infty} n(r) dz$, where $n(r)$ is the local density of the considered molecule at distance r from the nucleus. If we assume a Haser parent molecule distribution and neglect the photodestruction of the molecule, then:

$$F(x, y) = K \frac{1}{\sqrt{x^2 + y^2}} = \frac{K}{\rho},$$

ρ is in radians. K is a constant factor equal to:

$$K = \frac{h\nu A_{ul} p_u Q}{16\pi v_{\text{exp}} \Delta}.$$

Q is the gas production rate and v_{exp} is the gas expansion velocity. Δ is the geocentric distance. In polar coordinates in the Fourier ($u = \sigma \cos \alpha$, $v = \sigma \sin \alpha$) and image ($x = \rho \cos \theta$, $y = \rho \sin \theta$) planes, Eq.(1) reduces to:

$$\mathcal{V}(\sigma, \alpha) = \frac{cK}{\nu} \int_0^{+\infty} \int_0^{2\pi} A(\rho) \exp\left(-\frac{2i\pi\nu}{c} \rho\sigma \cos(\alpha - \theta)\right) d\theta d\rho. \quad (2)$$

It can be demonstrated that:

$$\int_0^{2\pi} \exp\left(-\frac{2i\pi\nu}{c} \rho\sigma \cos(\alpha - \theta)\right) d\theta = 2\pi J_0\left(\frac{2\pi\nu\rho\sigma}{c}\right),$$

where J_0 is the Bessel function of first kind and zero order. Therefore, Eq.(2) reduces to:

$$\mathcal{V}(\sigma, \alpha) = \frac{2\pi cK}{\nu} \int_0^{+\infty} A(\rho) J_0\left(\frac{2\pi\nu\rho\sigma}{c}\right) d\rho.$$

$\mathcal{V}(\sigma, \alpha)$ is a real function (a general property of the Fourier Transform of a symmetric function) of amplitude $\bar{\mathcal{V}}(\sigma) = \mathcal{V}(\sigma, \alpha)$, which can be also written:

$$\bar{\mathcal{V}}(\sigma) = \frac{c^2 K}{\nu^2} \times \frac{1}{\sigma} \int_0^{+\infty} A\left(\frac{c\rho}{2\pi\nu\sigma}\right) J_0(\rho) d\rho.$$

Let us call D the diameter of the antennas. For $\sigma/D \gg 0.2$ (typically $\sigma > 20$ m for 15-m dishes), the A term in the integral can be considered as unity. As $\int_0^{+\infty} J_0(\rho) d\rho = 1$, then:

$$\bar{\mathcal{V}}(\sigma) = \frac{hc^2 A_{ul} p_u Q}{16\pi\nu v_{\text{exp}} \Delta} \times \frac{1}{\sigma}. \quad (3)$$

This formula remains valid when photodissociation occurs, provided that $\sigma \gg c\Delta/\nu L$, where L is the photodissociation scale length.

In the same units (Jy km s^{-1}), the line area for autocorrelation (ON-OFF) spectra which corresponds to $\bar{\mathcal{V}}(0)$ is:

$$\bar{\mathcal{V}}(0) = \frac{hc A_{ul} p_u \mathcal{N}}{4\pi \Delta^2}, \quad (4)$$

where \mathcal{N} is the number of molecules sampled by the primary beam, which can be computed by volume integration.

REFERENCES

- Biver, N. 1997. Molécules mères cométaires: observations et modélisations. Ph.D. Thesis, University of Paris 7.
- Biver, N., and 22 colleagues 1999a. Long-term Evolution of the Outgassing of Comet Hale-Bopp From Radio Observations. *Earth Moon and Planets* 78, 5-11.
- Biver, N., and 13 colleagues 1999b. Spectroscopic Monitoring of Comet C/1996 B2 (Hyakutake) with the JCMT and IRAM Radio Telescopes. *Astronomical Journal* 118, 1850-1872.
- Biver, N., and 22 colleagues 2002. The 1995–2002 Long-Term Monitoring of Comet C/1995 O1 (Hale-Bopp) at Radio Wavelength. *Earth Moon and Planets* 90, 5-14.
- Bockelée-Morvan, D. 1987. A model for the excitation of water in comets. *Astronomy and Astrophysics* 181, 169-181.
- Bockelee-Morvan, D., Crovisier, J. 1989. The nature of the 2.8-micron emission feature in cometary spectra. *Astronomy and Astrophysics* 216, 278-283.
- Bockelée-Morvan, D., Crovisier, J. 2002. Lessons of Comet Hale-Bopp for Coma Chemistry: Observations and Theory. *Earth Moon and Planets* 89, 53-71.
- Bockelée-Morvan, D., Crovisier, J., Mumma, M.J., Weaver, H.A. 2004. The composition of cometary volatiles. In: Festou, M.C., Keller, H.U. Weaver, H.A. (Eds), *Comets II, The University of Arizona Press, Tucson*, 391-423.
- Bockelée-Morvan, D., Henry, F., Biver, N., Boissier, J., Colom, P., Crovisier, J., Despois, D., Moreno, R., Wink, J. 2009. Interferometric imaging of carbon monoxide in comet C/1995 O1 (Hale-Bopp): evidence of a strong rotating jet. *Astronomy and Astrophysics* 505, 825-843.
- Boissier, J., Bockelée-Morvan, D., Biver, N., Crovisier, J., Despois, D., Marsden, B.G., Moreno, R. 2007. Interferometric imaging of the sulfur-bearing molecules H₂S, SO, and CS in comet C/1995 O1 (Hale-Bopp). *Astronomy and Astrophysics* 475, 1131-1144.

- Boissier, J., Bockelée-Morvan, D., Rodionov, R. & Crifo, J.-F., 2010, First attempt at interpreting millimetric observations of CO in comet C/1995 O1 (Hale-Bopp) using 3D+t hydrodynamical coma simulations, *Astronomy and Astrophysics* 510, A24.
- Brooke, T.Y., Weaver, H.A., Chin, G., Bockelée-Morvan, D., Kim, S.J., Xu, L.-H. 2003. Spectroscopy of Comet Hale-Bopp in the infrared. *Icarus* 166, 167-187.
- Colom, P., Gérard, E., Crovisier, J., Bockelée-Morvan, D., Biver, N., Rauer, H. 1999. Observations of the OH Radical in Comet C/1995 O1 (Hale-Bopp) with the Nançay Radio Telescope. *Earth Moon and Planets* 78, 37-43.
- Combi, M.R., Kabin, K., Dezeew, D.L., Gombosi, T.I., Powell, K.G. 1999. Dust-Gas Interrelations In Comets: Observations And Theory. *Earth Moon and Planets* 79, 275-306.
- Cottin, H., Fray, N. 2008. Distributed Sources in Comets. *Space Science Reviews* 138, 179-197.
- Cottin, H., Bénilan, Y., Gazeau, M.-C., Raulin, F. 2004. Origin of cometary extended sources from degradation of refractory organics on grains: polyoxymethylene as formaldehyde parent molecule. *Icarus* 167, 397-416.
- Crovisier, J. 1987. Rotational and vibrational synthetic spectra of linear parent molecules in comets. *Astronomy and Astrophysics Supplement Series* 68, 223-258.
- Crovisier, J., Le Bourlot, J. 1983. Infrared and microwave fluorescence of carbon monoxide in comets. *Astronomy and Astrophysics* 123, 61-66.
- Dello Russo, N., DiSanti, M.A., Mumma, M.J., Magee-Sauer, K., Rettig, T.W. 1998. Carbonyl Sulfide in Comets C/1996 B2 (Hyakutake) and C/1995 O1 (Hale-Bopp): Evidence for an Extended Source in Hale-Bopp. *Icarus* 135, 377-388.
- Dello Russo, N., Mumma, M.J., DiSanti, M.A., Magee-Sauer, K., Novak, R., Rettig, T.W. 2000. Water production and release in comet C/1995 O1 Hale-Bopp. *Icarus* 143, 324-337.
- DiSanti, M.A., Mumma, M.J. 2009. Reservoirs for Comets: Compositional Differences Based on Infrared Observations. *Space Science Reviews* 138, 127-145.

- DiSanti, M.A., Mumma, M.J., Dello Russo, N.D., Magee-Sauer, K., Novak, R., Rettig, T.W. 1999. Identification of two sources of carbon monoxide in comet Hale-Bopp. *Nature* 399, 662-665.
- DiSanti, M.A., Mumma, M.J., Dello Russo, N., Magee-Sauer, K. 2001. Carbon Monoxide Production and Excitation in Comet C/1995 O1 (Hale-Bopp): Isolation of Native and Distributed CO Sources. *Icarus* 153, 361-390.
- DiSanti, M.A., Mumma, M.J., Dello Russo, N., Magee-Sauer, K., Griep, D.M. 2003. Evidence for a dominant native source of carbon monoxide in Comet C/1996 B2 (Hyakutake). *Journal of Geophysical Research (Planets)* 108, 5061.
- Eberhardt, P., and 10 colleagues 1987. The CO and N₂ Abundance in Comet P/ Halley. *Astronomy and Astrophysics* 187, 481-484.
- Farnham, T.L., Schleicher, D.G., Williams, W.R., & Smith, B.R. 1999, *BAAS*, 31, 3001
- Feldman, P.D., Cochran, A.L., Combi, M.R. 2004. Spectroscopic investigations of fragment species in the coma. In: Festou, M.C., Keller, H.U. Weaver, H.A. (Eds), *Comets II*, The University of Arizona Press, Tucson, 425-447.
- Fray, N., Bénilan, Y., Biver, N., Bockelée-Morvan, D., Cottin, H., Crovisier, J., Gazeau, M.-C. 2006. Heliocentric evolution of the degradation of polyoxymethylene: Application to the origin of the formaldehyde (H₂CO) extended source in Comet C/1995 O1 (Hale Bopp). *Icarus* 184, 239-254.
- Henry, F. 2003, *La comète Hale-Bopp à l'interféromètre du Plateau de Bure: étude de la distribution du monoxyde de carbone*, PhD Thesis, University of Paris 6
- Hu, H.-Y., Larson, H.P., Hsieh, K.C. 1991. Theoretical description of spectral line profiles of parent molecules in cometary comae. *Icarus* 91, 238-250.
- Huebner, W.F., Keady, J.J., Lyon, S.P. 1992. Solar photo rates for planetary atmospheres and atmospheric pollutants. *Astrophysics and Space Science* 195, 1-289.

- Greenberg, J.M., Li, A. 1998. From interstellar dust to comets: the extended CO source in comet Halley. *Astronomy and Astrophysics* 332, 374-384.
- Jorda, L., Gutiérrez, P. 2000. Rotational Properties of Cometary Nuclei. *Earth Moon and Planets* 89, 135-160.
- Jorda, L., Rembor, K., Lecacheux, J., Colom, P., Colas, F., Frappa, E., Lara, L.M. 1999. The Rotational Parameters of Hale-Bopp (C/1995 O1) from Observations of the Dust Jets At Pic du Midi Observatory. *Earth Moon and Planets* 77, 167-180.
- Lis, D.C., Bockelée-Morvan, D., Boissier, J., Crovisier, J., Biver, N., Charnley, S.B. 2008. Hydrogen Isocyanide in Comet 73P/Schwassmann-Wachmann (Fragment B). *Astrophysical Journal* 675, 931-936.
- Magee-Sauer, K., Mumma, M.J., DiSanti, M.A., Dello Russo, N.D., Rettig, T.W. 1999. Infrared Spectroscopy of the ν_3 Band of Hydrogen Cyanide in Comet C/1995 O1 Hale-Bopp. *Icarus* 142, 498-508.
- Meier, R., Eberhardt, P., Krankowsky, D., Hodges, R.R. 1993. The extended formaldehyde source in comet P/Halley. *Astronomy and Astrophysics* 277, 677-690.
- Milam, S. N., and 17 colleagues 2006. Formaldehyde in Comets C/1995 O1 (Hale-Bopp), C/2002 T7 (LINEAR), and C/2001 Q4 (NEAT): Investigating the Cometary Origin of H₂CO. *The Astrophysical Journal* 649, 1169-1177.
- Vasundhara, R., Chakraborty, P. 1999. Modeling of Jets from Comet Hale-Bopp (C/1995 O1): Observations from the Vainu Bappu Observatory. *Icarus* 140, 221-230.
- Zakharov, V., Bockelée-Morvan, D., Biver, N., Crovisier, J., Lecacheux, A. 2007. Radiative transfer simulation of water rotational excitation in comets. Comparison of the Monte Carlo and escape probability methods. *Astronomy and Astrophysics* 473, 303-310.

Table 1: Observed intensities of CO lines in single-dish (SD) and interferometric (Int.) modes.

Line	Mode	Beam	Intensity ^a (Jy km s ⁻¹)
$J(1-0)$	SD	41.8''	10.8 ± 0.43
	Int.	2.57'' × 3.58''	0.93 ± 0.04
$R_{1-0} = F_{\text{SD}}/F_{\text{Int}}$			11.6 ± 1.8 ^b
$J(2-1)$	SD	20.9''	82.8 ± 0.59
	Int.	2.0'' × 1.38''	4.65 ± 0.15
$R_{2-1} = F_{\text{SD}}/F_{\text{Int}}$			17.8 ± 3.8 ^b

^a From Bockelée-Morvan et al. (2009).

^b Include uncertainties in flux calibration: 10% for CO $J(1-0)$, 15% for CO $J(2-1)$ (Bockelée-Morvan et al. 2009).

Table 2: Modelled PdBI intensities of the CO lines in comet Hale-Bopp and slope of the visibility curves.

Model	$Q_{\text{CO}}^N:Q_{\text{CO}}^E$ ^a (%:%)	T (K)	v_{exp} (km s ⁻¹)	L_p (km)	F_{Int} (Jy km s ⁻¹)	R_{mod}	Slope ^b	$J(1-0)$		$J(2-1)$	
								$J(1-0)$	$J(2-1)$	$J(1-0)$	$J(2-1)$
Nuclear+Thin ^c	100:0	120	1.05	0	0.74	5.86	15.0	14.7	-1.02	-1.04	
Nuclear	100:0	120	1.05	0	0.70	4.25	15.7	19.1	-1.07	-1.20	
Nuclear	100:0	T_{var}^d	1.05	0	1.00	4.64	11.6	18.7	-0.96	-1.42	
Nuclear	100:0	120	v_{var}^e	0	0.78	4.77	13.6	17.2	-1.04	-1.21	
Nuclear	100:0	T_{var}^d	v_{var}^e	0	1.10	4.94	10.3	17.7	-0.95	-1.50	
Nuclear	100:0	T_{var}^d	v_{var}^e	0	1.09	5.38	10.7	16.3	-0.98	-1.35	
Extended	0:100	120	1.05	2000	0.32	1.31	32.2	55.8	-1.75	-1.96	
Extended	0:100	T_{var}^d	v_{var}^e	2000	0.53	2.27	19.6	34.3	-1.44	-1.82	
Composite	50:50	120	1.05	2000	0.51	2.92	20.8	26.5	-1.26	-1.35	
Composite	50:50	120	1.05	5000	0.44	2.60	23.3	27.5	-1.22	-1.26	
Composite	50:50	T_{var}^d	v_{var}^e	2000	0.84	3.89	13.0	21.3	-1.07	-1.51	
Composite	50:50	T_{var}^d	v_{var}^e	5000	0.72	3.48	14.3	21.9	-1.03	-1.40	
Composite	10:90	T_{var}^d	v_{var}^e	5000	0.37	1.76	25.4	37.7	-1.33	-1.53	

Footnotes to Table 2 :

^a Relative contribution (in percent) of the nuclear CO production rate Q_{CO}^{N} and extended CO production rate Q_{CO}^{E} to the total CO production rate $Q_{\text{CO}} = Q_{\text{CO}}^{\text{N}} + Q_{\text{CO}}^{\text{E}} = 2.1 \times 10^{30} \text{ s}^{-1}$.

^b Slope (i.e., power index) of the variation of the visibility amplitude with uv -radius between 20 and 150 m.

^c Opacity effects are not considered in radiative transfer calculations.

^d Variable kinetic temperature T_{var} : $T = 20 + 50 \times \log(r[\text{km}]/100)$ K for $100 < r < 10000$ km, $T = 120$ K for $r > 10000$ km, $T = 20$ K for $r < 100$ km.

^e Variable expansion velocity v_{var} : $v_{\text{exp}} = 0.9 + 0.15 \times \log(r[\text{km}]/1000)$ km s^{-1} for $r > 1000$ km, $v_{\text{exp}} = 0.9$ km s^{-1} for $r < 1000$ km.

^f Variable kinetic temperature $T_{\text{var(alt)}}$: $T = 20 + 50 \times \log(r[\text{km}]/100)$ K for $1500 < r < 10000$ km, $T = 120$ K for $r > 10000$ km, $T = 79$ K for $r < 1500$ km.

Table 3: CO IR line fluxes in March 1997.

Date	Line	Comment	Q_{CO} (s^{-1})	δDec^a ($''$)	$F_{\text{inner}}^{b,c}$ (W m^{-2})	$F_{\text{outer}}^{b,d}$ (W m^{-2})	$F_{\text{outer}}/F_{\text{inner}}$
3.80 March UT	R2	Measured ^b			43 ± 1.5	46.8 ± 2.9	1.09 ± 0.08
		Panel 3/Iso ^b	2×10^{30}	0	43.1/45.5	37.8/36.6	0.88/0.80
		Panel 3/Iso ^b	2×10^{30}	-1.2	40.7/39.1	37.4/35.8	0.92/0.92
		Panel 3/Iso ^b	2×10^{30}	-2.4	31.5/28.6	33.6/33.7	1.07/1.18
5.99 March UT	R6	Measured ^b			20.6 ± 1.6	21.4 ± 1.4	1.04 ± 0.11
		Panel 10/Iso ^b	2×10^{30}	0	36.9/34.9	31.2/26.1	0.85/0.75
		Panel 10/Iso ^b	2×10^{30}	-1.2	26.8/29.2	29.8/25.6	1.11/0.88
		Panel 10/Iso ^b	2×10^{30}	-2.4	20.9/20.6	26.7/24.1	1.28/1.17

^a Slit offset in declination. The slit is oriented East-West.

^b Measured intensities are from Brooke et al. (2003). Modelled intensities were computed using the brightness distributions of Panels 3 and 10 of Fig 11, for 3 and 5 March, respectively (first number in columns 6–8) and an isotropic model (referred to as Iso, second number in columns 6–8). A seeing of $1.78''$ and $1.7''$ (Brooke et al. 2003), for 3 and 5 March, respectively.

^c Line intensity in a $2'' \times 1''$ box in RA \times Dec centred on the peak of CO brightness along the slit.

^d Line flux in East-West averaged $5'' \times 1''$ boxes beginning $3''$ from peak.

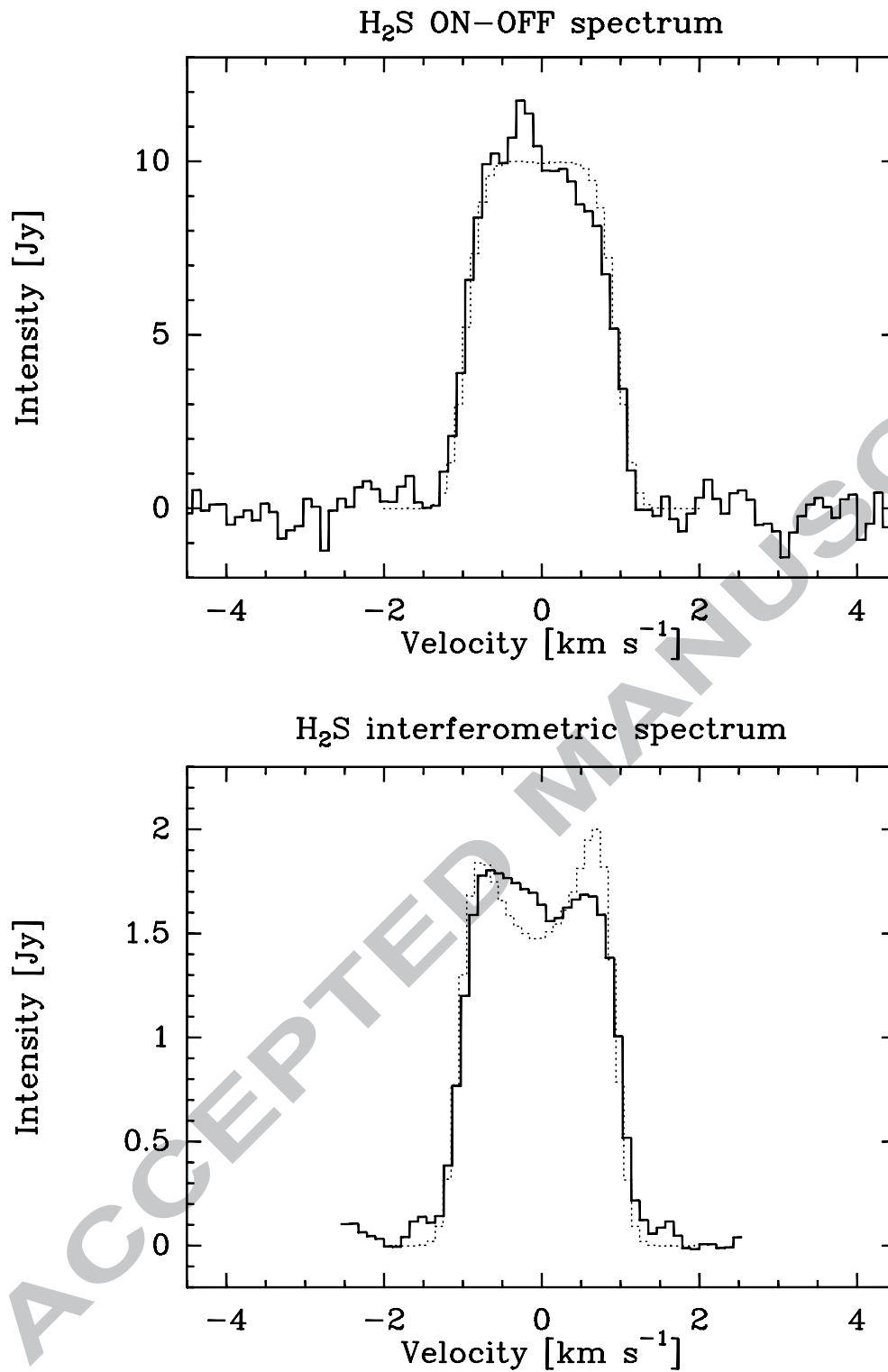


Fig. 1.— ON-OFF and interferometric spectra of the H₂S 2₂₀-2₁₁ line at 216.7 GHz obtained in comet Hale-Bopp on 13 March 1997 with the PdBI (Boissier et al. 2007). Synthetic spectra computed using the v_{var} law for the expansion velocity are shown with dotted lines. The angular resolution is 22.2'' and 1.7'', for the ON-OFF and interferometric beams, respectively.

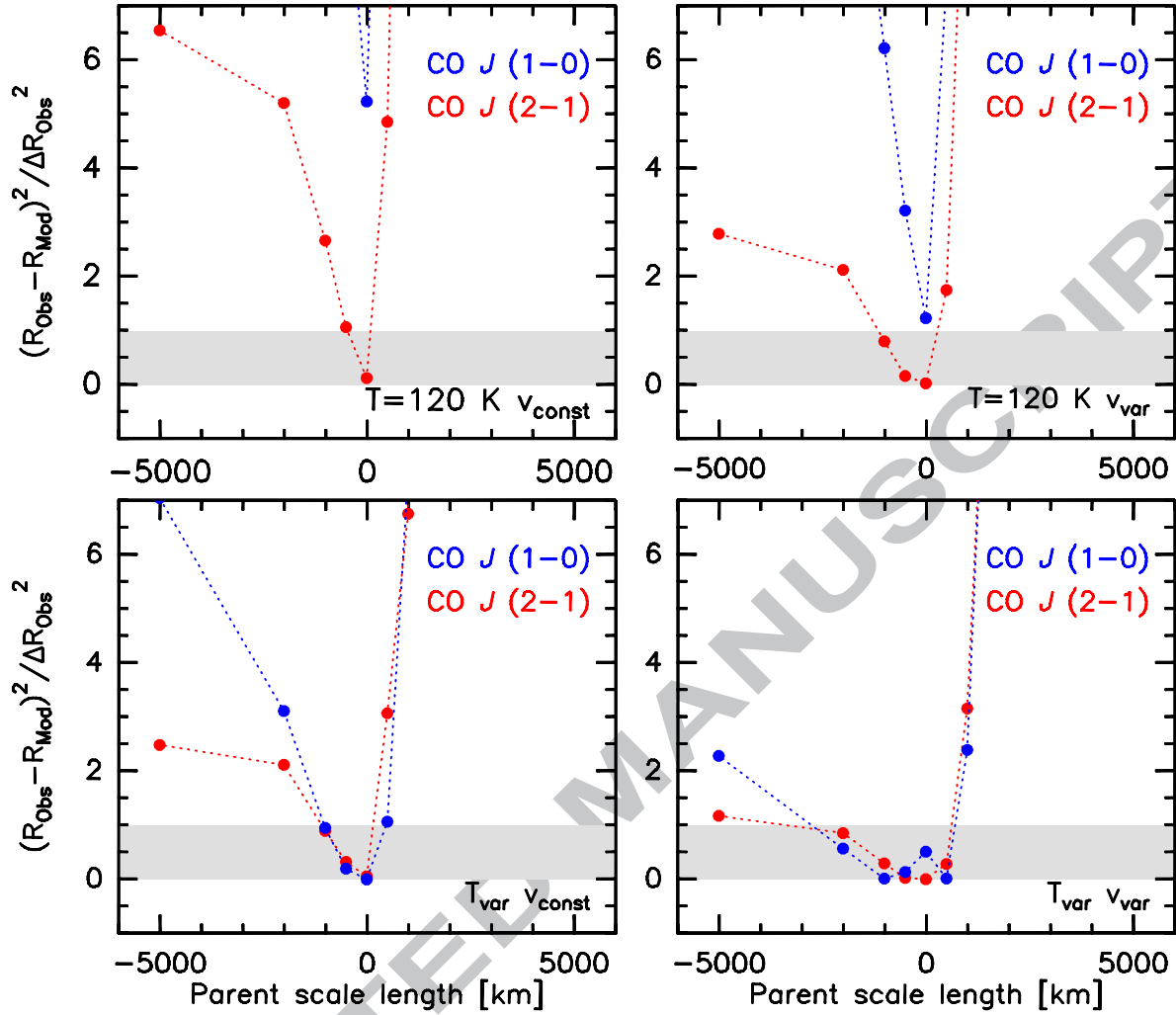


Fig. 2.— $\chi^2 = (R_{\text{Obs}} - R_{\text{Mod}})^2 / \Delta R_{\text{Obs}}^2$ as a function of the CO parent scale length, where R_{Obs} and R_{Mod} are the observed and modelled intensity ratios $R = F_{\text{SD}} / F_{\text{Int}}$, respectively, and ΔR_{Obs} is the error bar on R_{Obs} . Blue (respectively red) symbols are for the CO $J(1-0)$ (respectively $J(2-1)$) lines. Results plotted in the right part of the plots (positive scale lengths) are for pure extended distributions (i.e., $Q_{\text{CO}}^N : Q_{\text{CO}}^E = (0:100)$). Results for composite distributions ($Q_{\text{CO}}^N : Q_{\text{CO}}^E = (50:50)$) are shown in the left part of the plot (negative scale lengths). The grey region corresponds to $0 < \chi^2 < 1$. The four quadrants correspond to different gas temperature and velocity laws indicated in the bottom right corner.

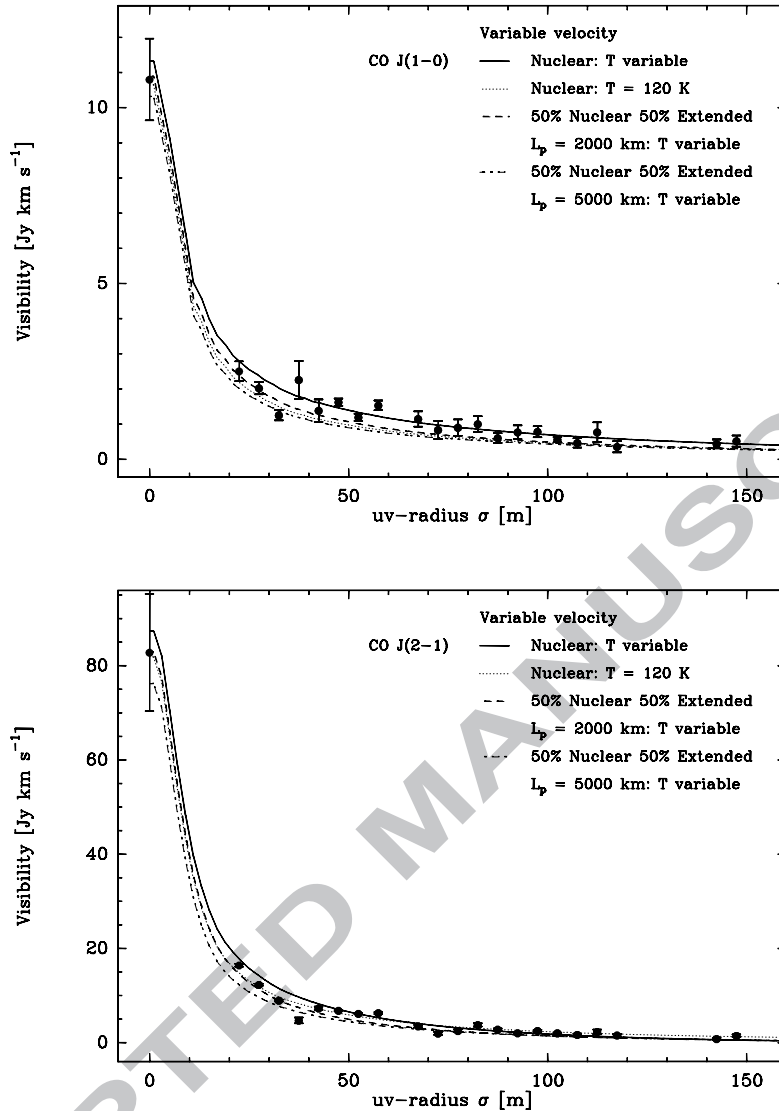


Fig. 3.— Amplitude of the visibility as a function of uv -radius for the CO $J(1-0)$ line (top) and the CO $J(2-1)$ line (bottom). Measurements are shown by dots with error bars which correspond to statistical noise uncertainties, except for the ON-OFF measurements where calibration uncertainties (10% and 15% for $J(1-0)$ and $J(2-1)$, respectively) are added quadratically. The different curves correspond to different models: nuclear production with variable gas temperature in the coma (plain line), nuclear production with constant temperature (dotted line), combined nuclear/extended productions in ratio 50:50 with $L_p = 2000$ km and variable temperature (dashed line), combined nuclear/extended productions in ratio 50:50 with $L_p = 5000$ km and variable temperature (dotted-dashed line). All models consider isotropic outgassing at a velocity described by v_{var} and a total CO production rate $Q_{\text{CO}} = 2.1 \times 10^{30} \text{ s}^{-1}$.

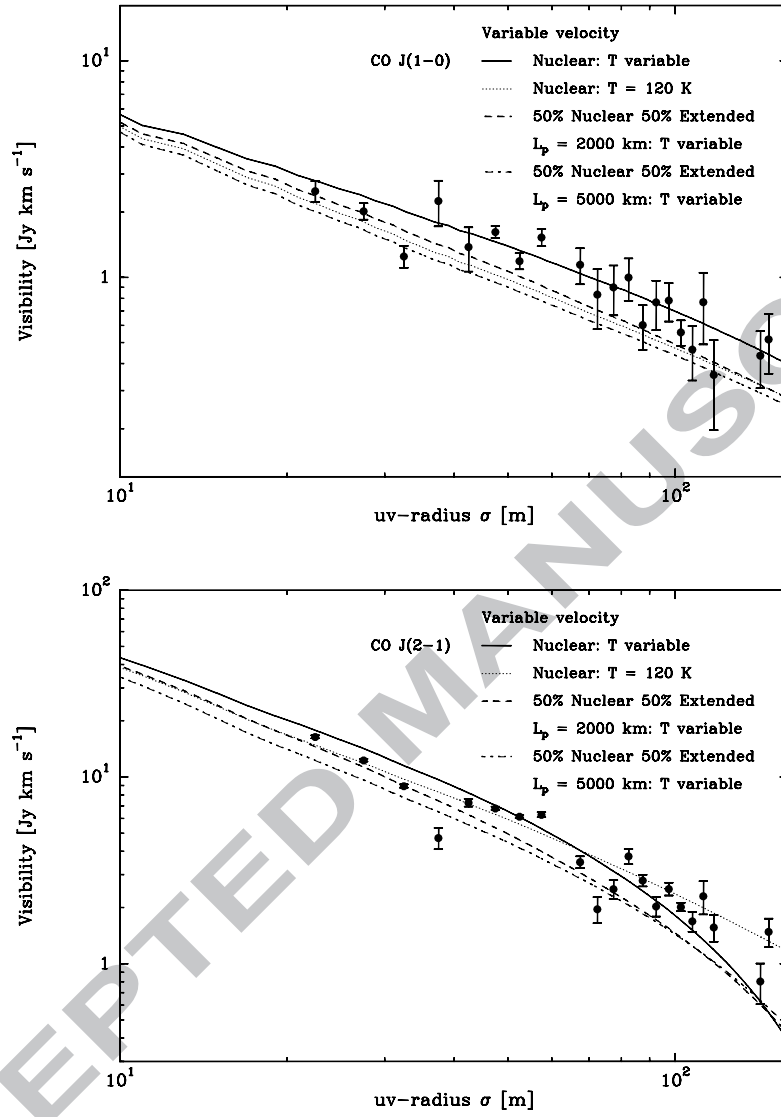


Fig. 4.— Log-Log plot of the amplitude of the visibility as a function of uv -radius for the CO $J(1-0)$ line (top) and the CO $J(2-1)$ line (bottom). Model parameters are the same as for Fig. 3.

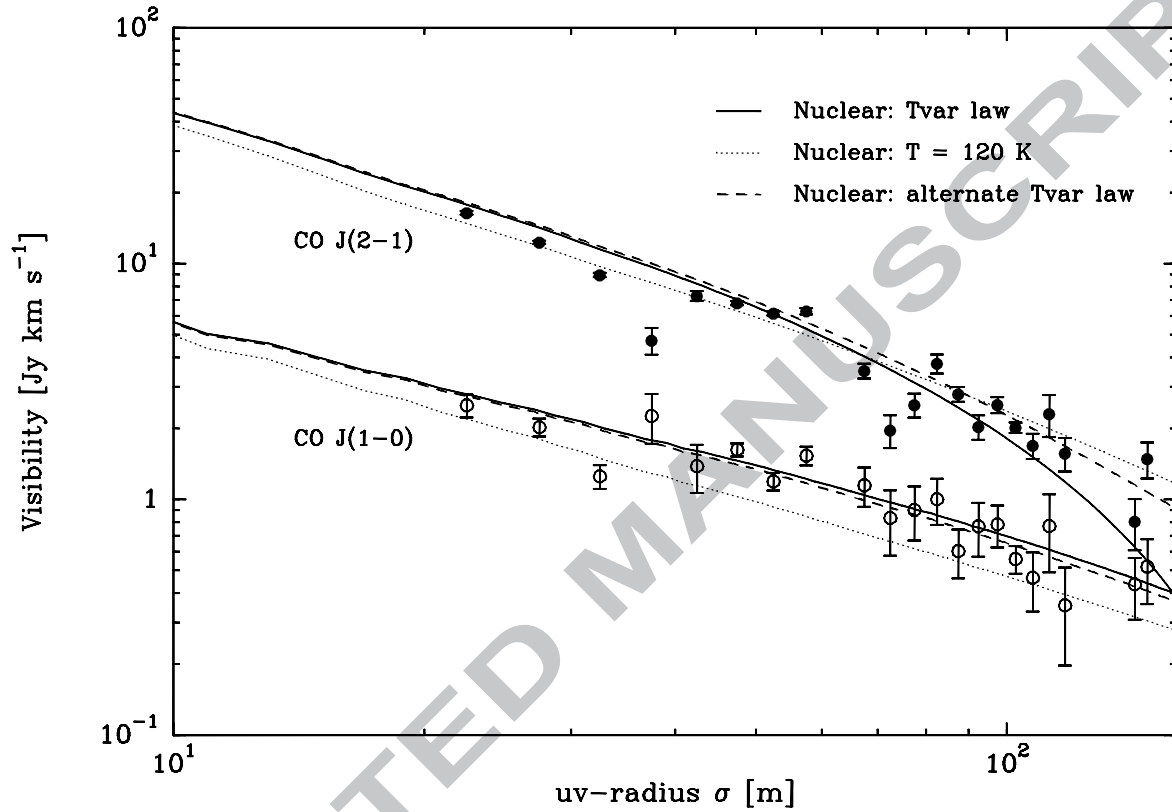


Fig. 5.— Amplitude of the visibility as a function of uv -radius. CO $J(1-0)$ (respectively $J(2-1)$) measurements are shown with open (respectively filled) symbols with error bars. The different curves correspond to calculations for a CO nuclear production and different temperature laws. Other model parameters are the same as for Fig. 3.

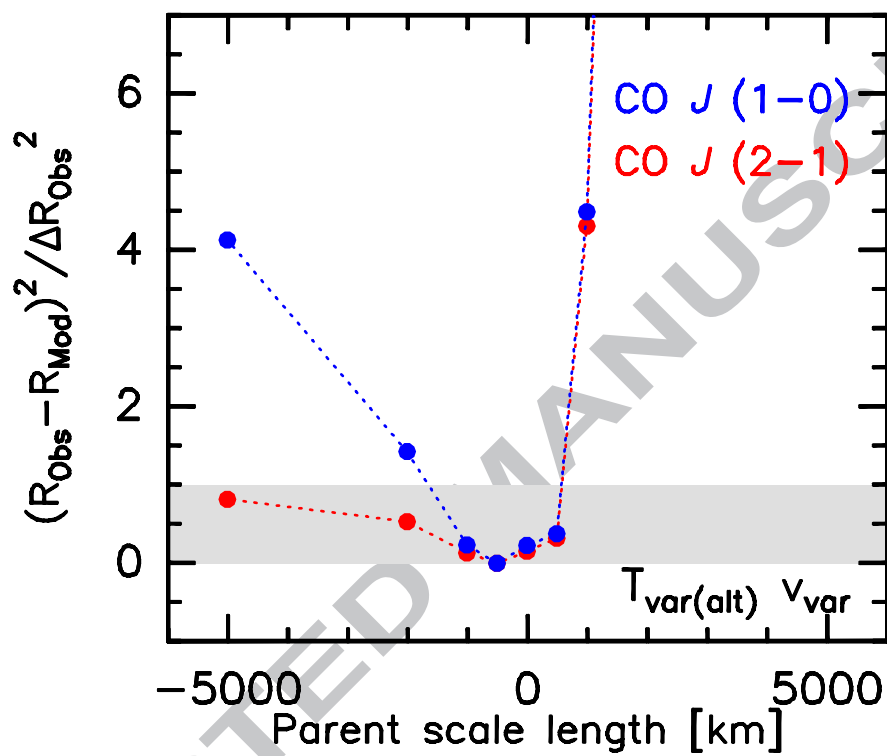


Fig. 6.— Same as Fig. 2, using the $T_{\text{var}(alt)}$ and v_{var} laws

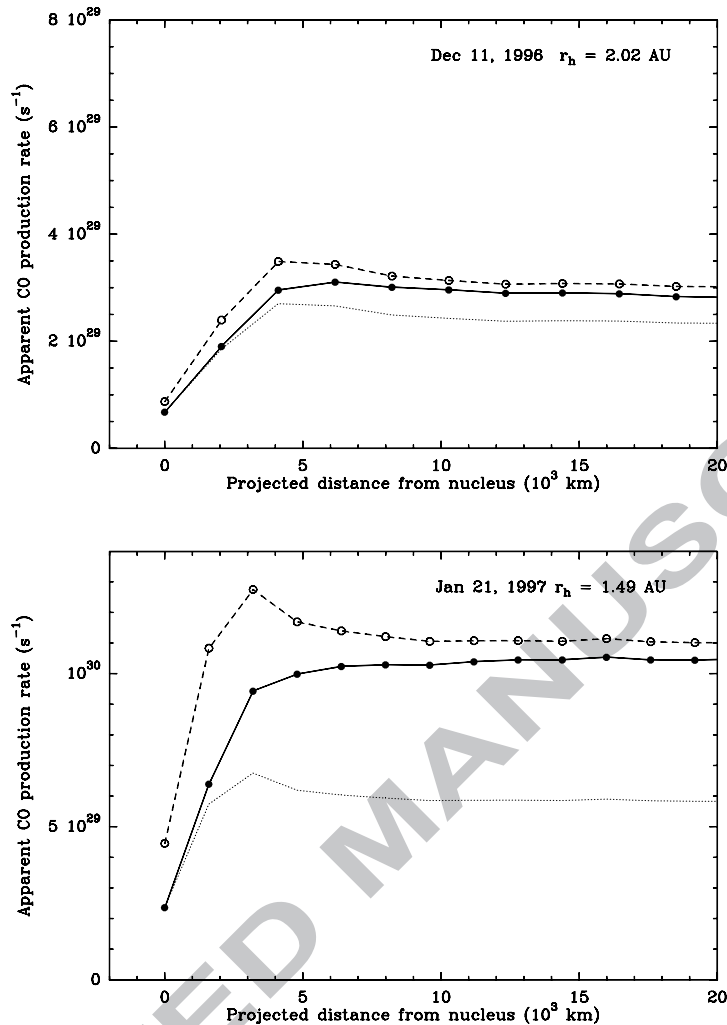


Fig. 7.— Q -curves generated with the isotropic model of CO $v = 1-0$ line emission. CO is assumed to be released from the nucleus. Lines used are R2, R3, P2 and P3 (Dec. data), R0, R1, P1, R2, P2, R3, P3, R4, R5, R6 (Jan. data). The aperture is set to $1'' \times 1''$. These Q -curves can be directly compared to Fig. 7 of DiSanti et al. (2003). Plain symbols: results with all processes included (optical depth effects, full rotational and vibrational excitation model). Open symbols: reference Q -curve, i.e., model results under optically thin conditions, assuming Boltzmann rotational level populations and ineffective vibrational collisional relaxation. Dotted curve: optically thin Q -curve scaled to the value of the optically thick Q -curve at the nucleus position. Calculations were performed with $T = 60, 80$ K, and $v_{exp} = 0.9, 1.0$ km s^{-1} , for December 11, 1996, and January 21, 1997 conditions, respectively

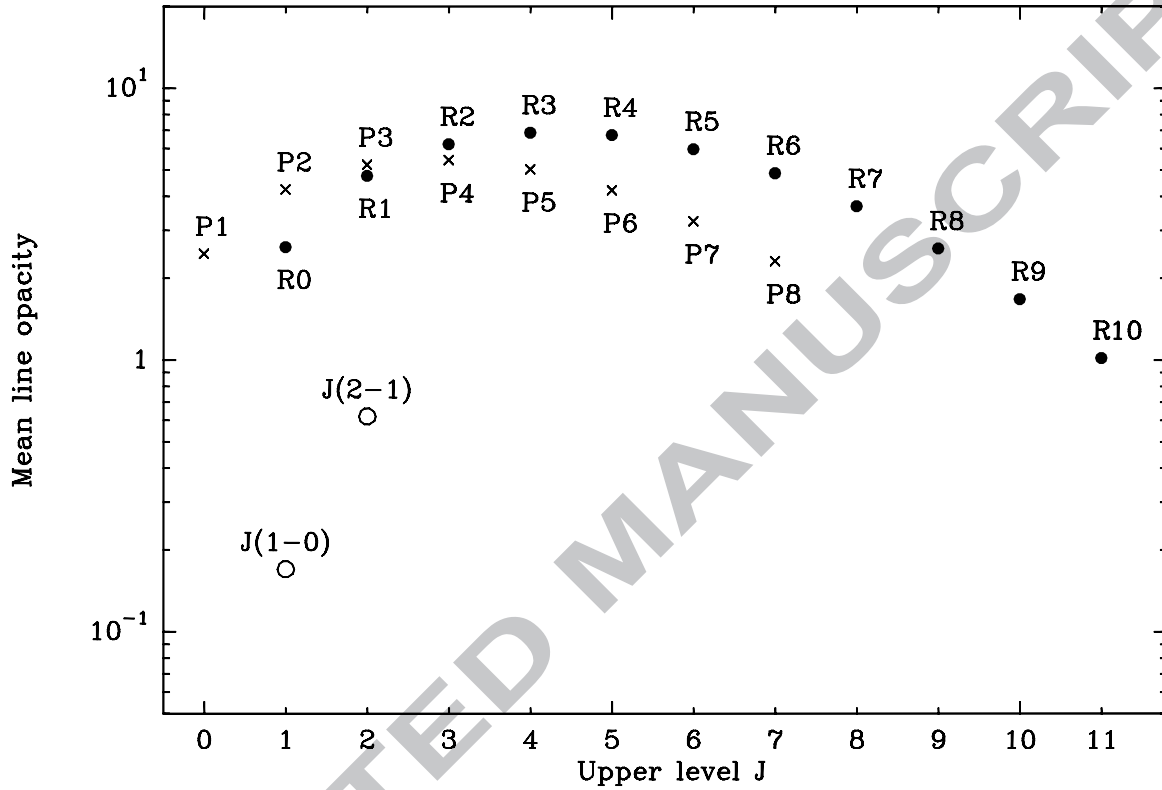


Fig. 8.— Mean opacity of observed CO IR lines for conditions of early-March 1997 ($\Delta = 1.47$ AU, $Q_{\text{CO}} = 2 \times 10^{30} \text{ s}^{-1}$, $T = 90$ K, $v_{\text{exp}} = 1.1 \text{ km s}^{-1}$). Calculations are for a circular aperture of $1''$ diameter centred on the nucleus. The mean opacities of the 115 and 230 GHz lines in the same FOV are plotted, for comparison.

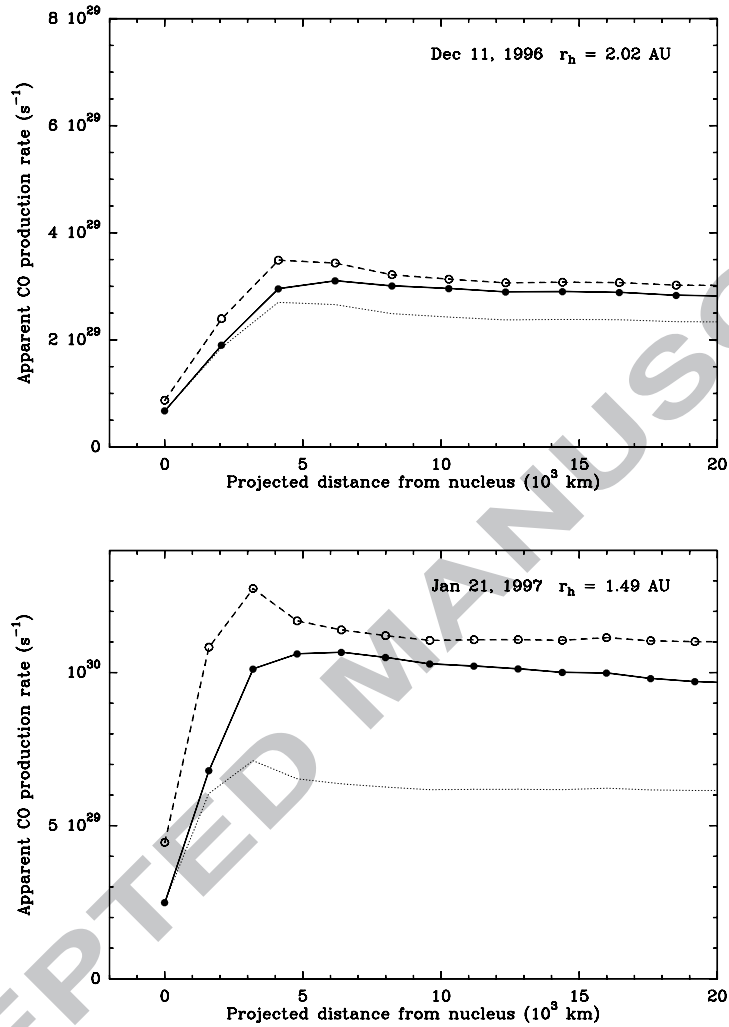


Fig. 9.— Same as Fig. 7 with gas acceleration considered in radiation transfer calculations. Apparent CO production rates were computed assuming a constant outflow velocity $v_{exp} = 0.9$ and 1.0 $km\ s^{-1}$, for 11 December 1996, and 21 January 1997, respectively.

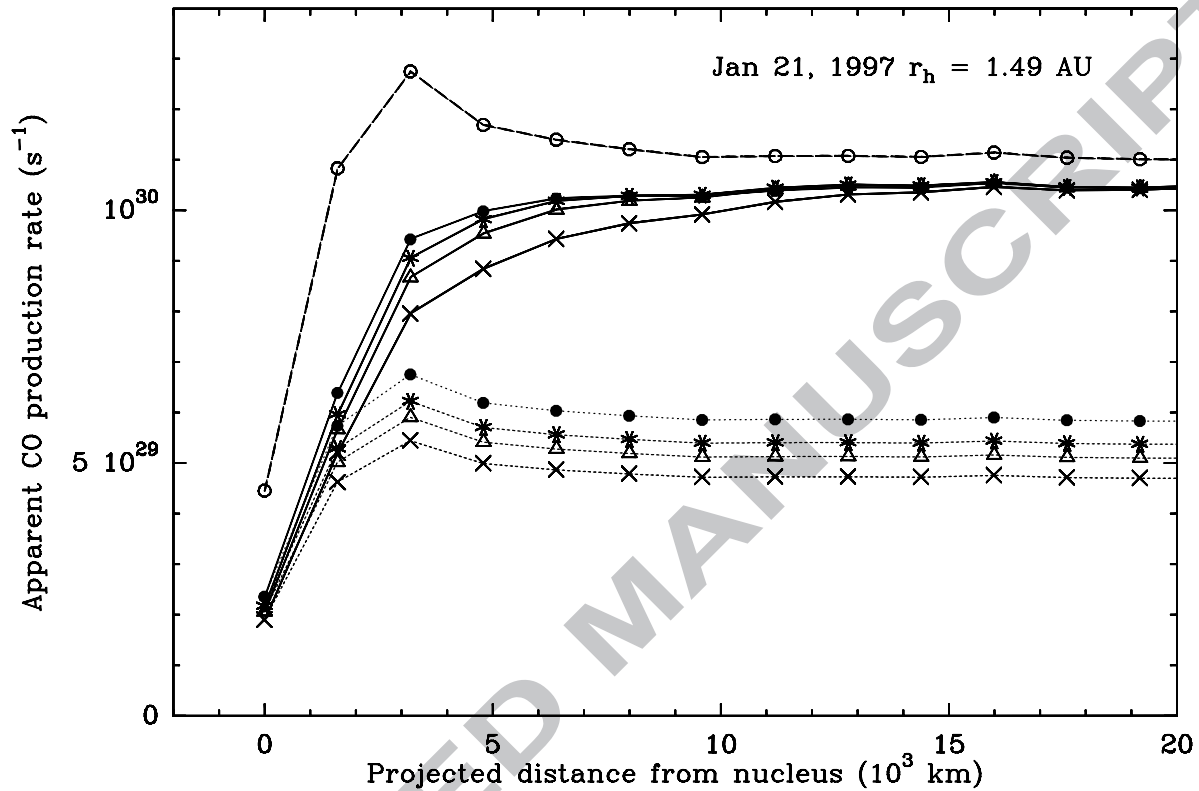


Fig. 10.— Same as Fig. 7 for January 21, 1997, considering both pure nuclear production and combined (50:50) nuclear/extended distributions: nuclear (filled dots), combined with $L_p = 1500$ km (stars), 2500 km (empty triangles) and 5000 km (crosses). The reference Q -curve is shown by empty circles connected by dashed lines, as in Fig. 7. Scaled reference Q -curves are shown with dotted lines. Other model parameters are the same as for the calculations shown in Fig. 7.

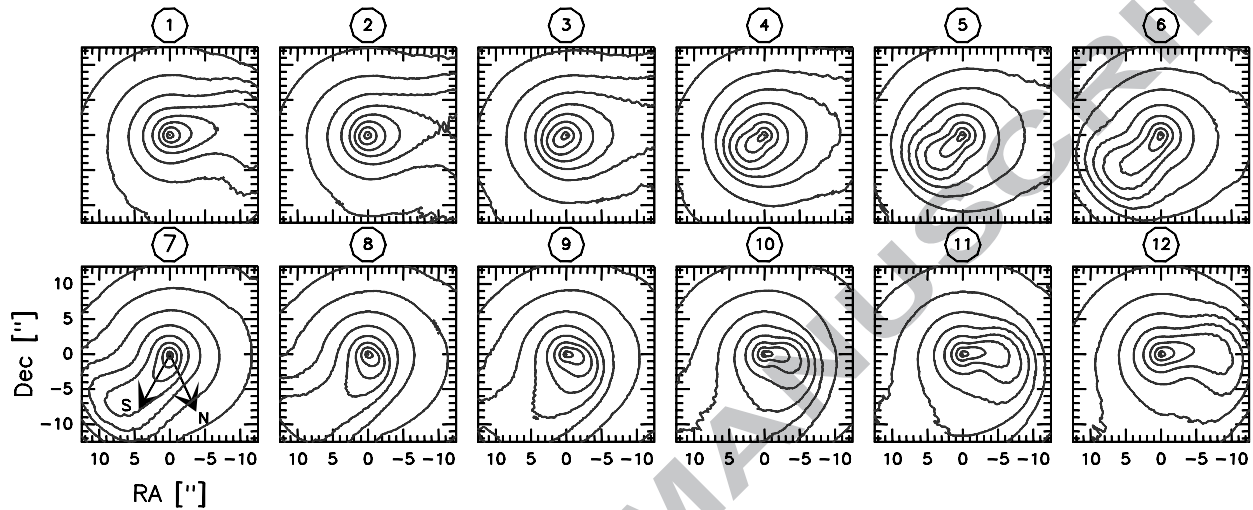


Fig. 11.— Time evolution of the brightness distribution (not corrected for seeing) of the $v = 1-0$ R6 CO line for geometrical conditions of 1–5 March 1997. The coma model of Bockelée-Morvan et al. (2009) is used (jet model (3); $Q_{\text{CO}} = 2 \times 10^{30} \text{ s}^{-1}$). The gas coma temperature is taken equal to 90 K. Panels 1 to 12 cover one rotation period $P = 11.35$ h with a time step of $P/12$. Line fluxes were computed for $0.2 \times 0.2''$ pixel size. Contour levels are in logarithmic scale and spaced by 0.15. Maximum fluxes on the maps are between 9.2 and $9.6 \cdot 10^{-18} \text{ W m}^{-2}$. The nucleus North pole (N) and the Sun (S) directions are indicated. Celestial East is on the left.

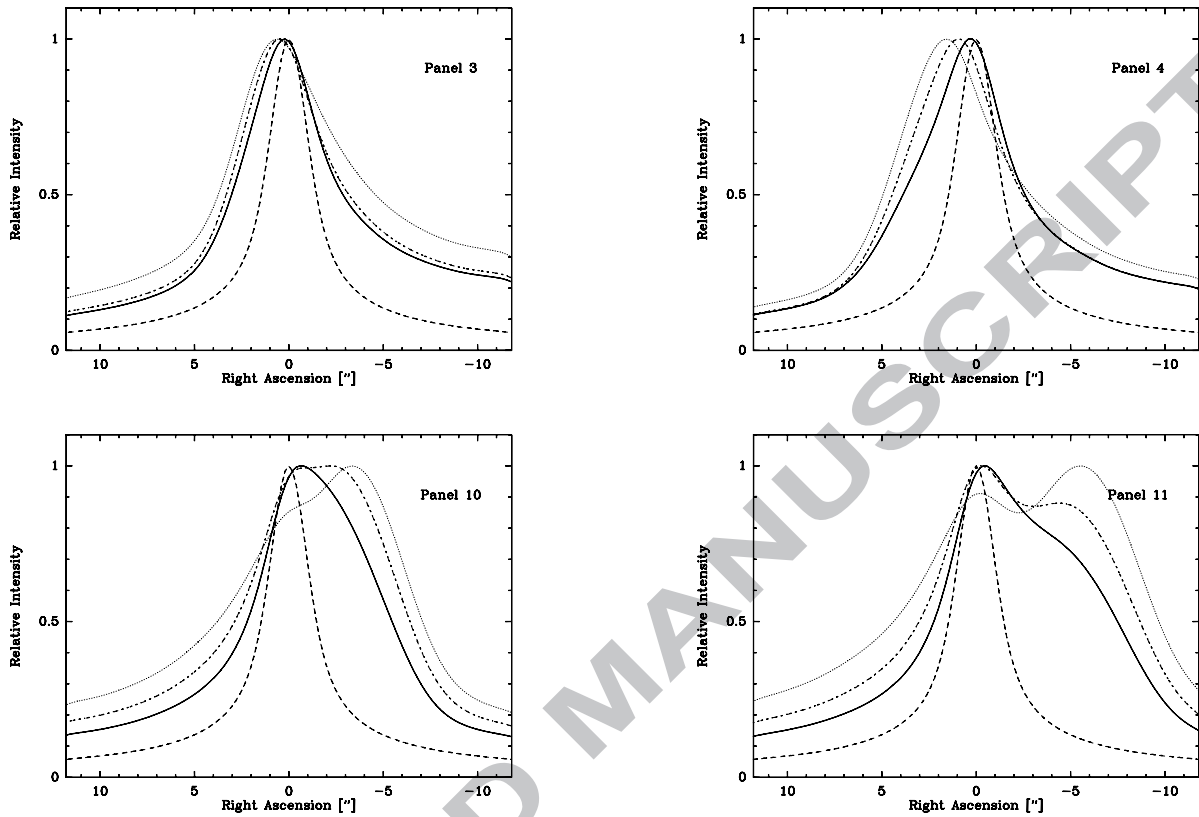


Fig. 12.— CO $v = 1-0$ R6 spatial profiles derived from the brightness maps (Panels 3, 4, 10, and 11) shown in Fig. 11 convolved with the PSF. Extractions are parallel to the RA axis and centred at $\delta\text{Dec} = 0''$ (plain line), $\delta\text{Dec} = -1.2''$ (dashed-dotted line) and $\delta\text{Dec} = -2.5''$ (dotted line). Intensity has been integrated over rectangular boxes of $1''$ along Dec axis and $0.2''$ along RA axis. The dashed line shows a ρ^{-1} column density profile convolved with the PSF. The seeing was taken equal to $1.7''$. Peak intensities (units of $10^{-17} \text{ W m}^{-2}$) are 3.5, 3.2, 2.4 (Panel 3), 3.5, 3.4, 2.8 (Panel 4), 3.4, 2.7, 2.1 (Panel 10), and 3.3, 2.6, 1.9 (Panel 11) for $\delta\text{Dec} = 0, -1.2'',$ and $-2.4'',$ respectively.

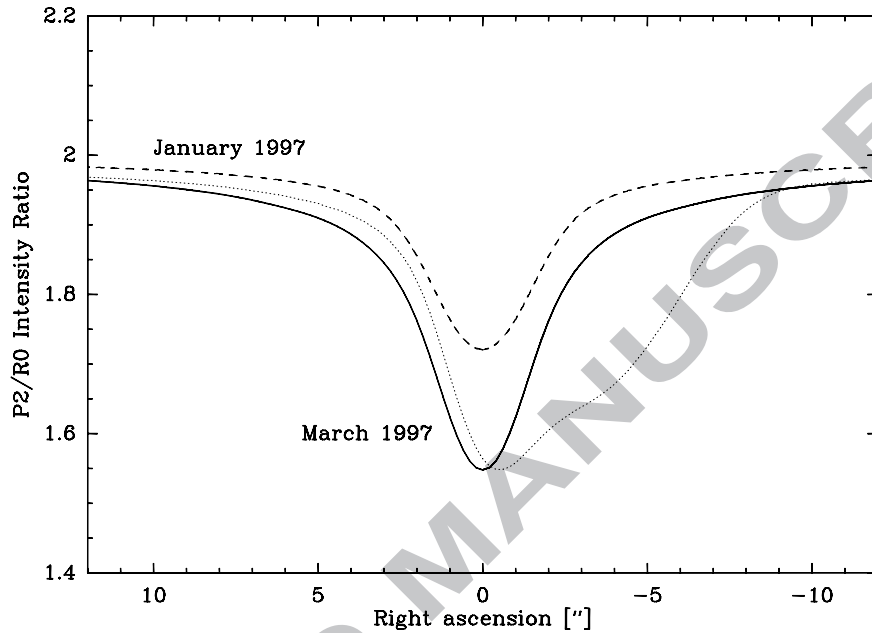


Fig. 13.— Ratio of the P2 to R0 line intensities along a slit aligned along the RA axis and centred on the nucleus. Results from radiative transfer calculations in an isotropic coma are shown in dashed (parameters of 21 Jan. 1997) and plain (early March 1997) lines. Results obtained with the jet model (phase of panel 10) are shown in dotted lines. The ratio was computed using PSF-corrected intensities over rectangular boxes of 1" along Dec axis and 0.2 " along RA axis.